Coupling of spallation and microjetting in aluminum at the atomic scale

Xin Yang [1], Yu Tian [2,*], Han Zhao [3], Fang Wang [4,†], Lusheng Wang [5], Moujin Lin [1], Peng Wen [1], and Wenjun Chen [6]

[1] *School of Environment and Resource, Southwest University of Science and Technology, Mianyang, Sichuan 621010, People's Republic of China*

[2] *National Engineering Research Center of Die and Mold CAD, School of Materials Science and Engineering, Shanghai Jiao Tong University, Shanghai 200240, People's Republic of China*

[3] *School of Intelligent Manufacturing, Chengdu Technological University, Chengdu 611730, People's Republic of China*

[4] *School of Materials and Energy, Southwest University, Chongqing 400715, People's Republic of China*

[5] *College of Mechanical Engineering, Chongqing University of Technology, Chongqing 400054, People's Republic of China*

[6] *Faculty of Intelligence Manufacturing, Yibin University, Yibin 644000, Sichuan Province, People's Republic of China*

(Received 20 March 2024; revised 30 June 2024; accepted 9 July 2024; published 30 July 2024)

Nonequilibrium molecular dynamics simulations were carried out to explore the coupling behaviors of spallation and microjetting in single-crystal (SC) and nanocrystalline (NC) Al at the atomic scale. Both SC and NC models exhibited void collapse, serving as an indispensable element complementary to the classical ductile fracture mechanisms dominated by nucleation, growth, and coalescence. Two representative mechanisms—compressive collapse and spontaneous collapse—were uncovered, with a unique behavior in which a coalesced void also collapsed. It was also discovered that the spallation might either cause the microjet to disappear or accelerate fragmentation, with the disappearance effectuating a peculiar transformation from coexisting spallation and microjetting to pure spallation. The difference between SC and NC microjetting models residing in that grain boundary not only caused a larger peak velocity of the spike tip due to the inhomogeneous deformation but also restrained the Richtmyer-Meshkov instability growth to some extent owing to energy dissipation. The jet sheet fragmentation was attributed to three mechanisms: void nucleation, growth, and coalescence for the jet body; longitudinal necking induced by the tensile stress for the residual one-dimensional jet body; and transverse necking induced by the shear and tensile stresses for the jet head.

DOI: 10.1103/PhysRevB.110.024113

I. INTRODUCTION

Dynamic mechanic characteristics and responses of materials in extreme conditions, like high pressure, high temperature, and high strain rate, have garnered a great deal of attention in several fields such as shock wave physics and inertial confinement fusion [1]. Under these severe conditions, the dynamic mechanical properties of ductile metal materials must be influenced. Therefore, it is vitally important to investigate the evolutionary processes and underlying mechanisms of dynamic damage and fracture.

Spallation and microjetting, being two primary failure behaviors, represent pressing scientific problems within the fields of weapon science and material dynamics. As is well known, the dynamic response of materials has brought difficulties in fine measurement of the evolutionary processes of internal and external microstructures. Thus, researchers have developed a series of measurement techniques. Some direct measurement technologies, like x-ray photography [2], proton photography [3], and metallographic examination of recovered samples [4,5], are used to provide insight into the damage process within the material. Material failure information may also be acquired indirectly by monitoring the free surface velocity history of the sample [6]. It is possible to observe the intricate fragmentation process at the surface as well as the subsequent transportation and mixing of the broken material using testing technologies [7], such as x-ray photography [2,8], Asay foil [9], piezoelectric pins [10], photon Doppler velocimetry [11], Mie scattering [12], and holography [13].

Even with the significant advancements in experimental methodologies, many phenomena remain unobservable, and underlying physical mechanisms remain challenging to resolve through experimentation. In recent years, molecular dynamics (MD) simulation has progressively become an indispensable tool for experimental research because of its unique advantages in elucidating the dynamic evolution of microstructures, such as overcoming the technological barriers to experiment and providing a microscopic comprehension of spallation and microjetting processes. Thus, compared with physical experiments, MD simulations are ideally suited for studying the microscopic damage and fracture behaviors of ductile metals.

Spallation is microscopically characterized by nucleation, growth, and coalescence of voids in ductile metal [14,15]. Damage to fracture is strongly influenced by external loading conditions (loading mode, shock pressure, ambient temperature, etc.) [16,17] and internal factors of the material (grain boundary type, grain size, void, etc.) [18–20]. These factors may affect the development of stress concentration, which is responsible for the void nucleation site, growth size,

*Contact author: tian.y@sjtu.edu.cn

†Contact author: wangfang_cq1978@163.com

and coalescence manner [21]. In addition to void nucleation, growth, and coalescence, another intriguing behavior is void collapse observed in dynamic triaxial tension and spallation processes [22,23]. Here, it should be emphasized that the term *void collapse* in this paper does not refer to that in porous material under compression waves but to that in the original defect-free material under the dynamic tensile process. Although the collapse behavior is ascertained, the collapse mechanism further needs to be explored.

A microjet may generate at the defective free surface due to the reflection of the strong compressive wave at the metal/vacuum or metal/gas interface. In theory, a microjet is a specific limiting case of Richtmyer-Meshkov instability (RMI) in both solid and liquid media. The formation of a microjet is heavily influenced not only by different surficial defects but also by loading conditions, like the waveform [24,25], peak pressure [26], second shock [27,28], and ambient temperature [29]. Once the material is ejected from the defective surface, the microjet enters the stages of transport, breakup, and conversion [30]. It has been revealed that the formation of a microjet is a layered aggregation process from the surficial layer of a defect to its inner layer, which is independent of the defect type [26,31]. Since present equipment struggles to capture the experimental process, macro- and micro-scaled numerical simulations [26,31,32] have increasingly become a standard supplement for investigating the evolution laws, particularly in the macrodynamic phenomena and micromechanisms of breakup and conversion. Some important characteristics, like the particle velocity and temperature distributions of the ejecta along the shock direction [26], jet tip velocity history [26,33], and mass (or volume)-velocity and size-velocity distributions [34], have been examined in detail. Phenomenally, it is observed that breakup is caused by necking for the one-dimensional jet and void growth and coalescence for the two-dimensional jet [26,35]. Indeed, jet breakup is influenced by perturbations in velocity, temperature, and pressure, with the velocity perturbation being the most significant. It has also been discovered that the ejecta size obeys a power-law distribution for small-sized fragments and an exponential distribution for big ones [36].

For now, the consensus is that, in most studies, spallation and microjetting are independent. Spallation and microjetting can occur simultaneously under certain conditions, as confirmed by experiments [2] and numerical simulations [25,37]. The concurrent events can be classified into three types: the generation of spallation on both sides of the microjet [37], the generation of spallation behind the microjet tail [25], and the combination of the previous two types [38]. Unfortunately, there is not much emphasis placed on the coupling behavior between spallation and microjetting. Furthermore, there are still some aspects needed for an in-depth examination. For example, previous researchers have focused on the breakup process of the microjet body, but they do not reveal the breakup mechanism of the two-dimensional jet head. Furthermore, it is also important to clarify how spallation and microjetting evolution are mutually influenced. Additionally, to our limited knowledge, it appears that the nanocrystalline (NC) material is not applied in previous studies of microjetting. Thus, the effect of the grain boundary on microjet evolution will be examined in this paper.

In this paper, we use the MD approach to probe dynamic responses and damage mechanisms of spallation and microjetting in single-crystal (SC) and NC Al, paying particular attention to the damage evolution and the interaction between spallation and microjetting. This paper is arranged as follows: Sec. II briefly describes MD simulation details of spallation and microjetting, followed by the corresponding simulation results and analyses in Sec. III. Section IV addresses the discussion about the interaction between spallation and microjetting. Finally, several important findings are concluded in Sec. V.

II. MD SIMULATION DETAILS

In this paper, the open-source MD simulator LAMMPS was utilized to perform the spallation and microjetting of SC and NC Al. The interaction between Al atoms is described by the potential function developed by Winey *et al.* [39]. Yang *et al.* [40] validated the dynamic applicability of this potential via the Hugoniot curve, and it was also proved to be capable of providing an accurate description of dynamic damage at high strain rates.

Table I shows the details of the model. Based on the spallation model, the microjetting model with a sinusoidal surface was built by deleting some atoms at the right side of the model. The MD models are provided in Fig. S1 in the Supplemental Material [41]. The initial perturbation of the rear free surface is described by a sine function $y = \zeta_0 \sin(kx)$, where ζ_0 is the initial perturbation amplitude, $k = 2\pi/\lambda_0$ is the wave number, and λ_0 is the perturbation wavelength. In microjetting models, ζ_0 is 3.23 nm, λ_0 is 11.80 nm, k is $\sim 0.53\,\mathrm{nm}^{-1}$, and $k\zeta_0$ is 1.72. The NC model was created by ATOMSK software using the Voronoi technique, and the average grain size was 16.86 nm.

The piston-target method was used to perform the spallation and microjetting of SC and NC Al through nonequilibrium MD simulations. The loading end was on the left side of the model, while the free surface was on the right. Before the piston impact, periodic boundary conditions were applied to the three directions of the model, and the energy of the model was minimized through the conjugate gradient method. The model was then allowed to relax enough at 300 K for 30 ps using an isothermal-isobaric (NPT) ensemble to achieve a condition where the residual stress of the system could be ignored. After that, the NPT ensemble was changed to the microcanonical (NVE) ensemble, with the free boundary condition replacing the periodic boundary condition of the system in the y-axis direction ([010]). A rigid piston assigned with an initial velocity u_p of 1–5 km/s impacted the target along the Y-axis direction. The target was loaded for 10 ps before being released, removing the interaction between the piston and the target to achieve the unloading. The unloading time was 90 ps, and the time step was 1.0 fs throughout the simulation process. Additionally, all MD simulation results were postprocessed using the OVITO program.

III. RESULTS AND ANALYSES

A. Spallation behaviors

It is commonly accepted that the spallation fracture is characterized by void nucleation, growth, and coalescence.

TABLE I. Model parameters and setups.

Case	Model	Model size ($X \times Y \times Z$, nm^3)[a]	Atom amount ($\times 10^6$)	Defect type
Spallation	SC	24.3 × 149.0 × 24.3	5.30	None
	NC	24.3 × 160.9 × 24.3	5.76	
Microjetting	SC	24.3 × 149.0 × 24.3	5.19	Sinusoidal perturbation
	NC	24.3 × 148.0 × 24.3	5.18	

[a]The X, Y, and Z axes of the model correspond to the [100], [010], and [001] crystal orientations.

Thus, probing the dynamic ductile fracture mechanism in the SC and NC Al models requires in-depth knowledge of void evolution.

In Fig. 1(a), a single nucleated void emerged at $t = 35.0$ ps; a few randomly distributed voids were presented in the spallation zone at $t = 37.0$ ps, and their further growth resulted in the formation of the first spallation zone at $t = 40.0$ ps. As the reflected stress wave from the free surface propagated back to the loading end, the interaction of two rarefaction waves led to the occurrence of some additional voids at $t = 52.0$ ps. Some more tiny voids appeared toward the loading end due to the further propagation of the rarefaction wave at $t = 55.0$ ps. Simultaneously, the previously nucleated voids grew, causing the formation of the second spallation zone. Additionally, the voids were substantially more in the second spallation zone than in the first one. In Fig. 1(a), the voids in the NC model

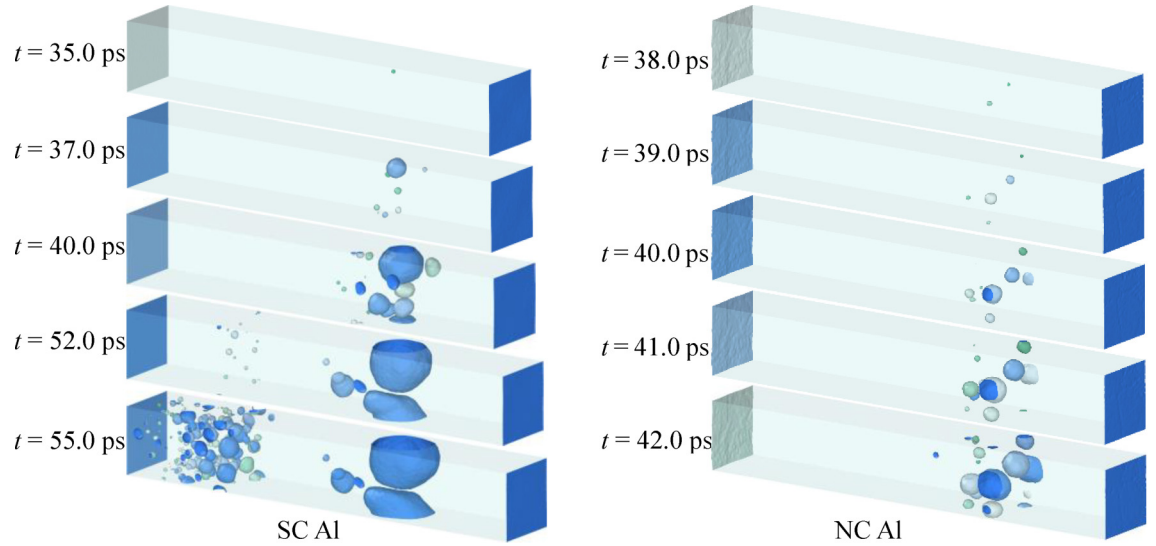

(a) $u_p = 1$ km/s

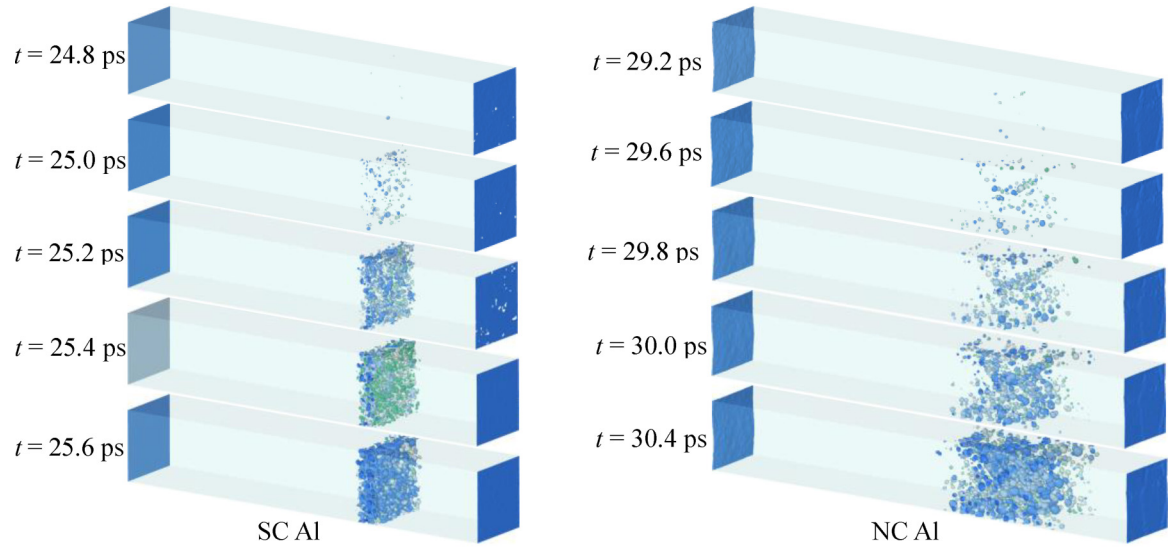

(b) $u_p = 2$ km/s

FIG. 1. Void nucleation and growth during the primitive stage of the spallation at $u_p = 1$ and 2 km/s.

were also relatively less in the spallation zone throughout the nucleation and growth (NAG) processes, and no second spallation formed. In Fig. 1(b), the voids in the SC model were extremely concentrated in the spallation zone at $u_p =$ 2 km/s, but the voids in the NC model were somewhat dispersed because of the grain boundary. In comparison with the SC model, the NC model had a significantly higher void number. Additionally, the sequential snapshots of void evolution at $u_p = 3-5$ km/s can be seen in Fig. S2 in the Supplemental Material [41].

The void nucleation site and growth manner have been previously studied [40], but void collapse behavior remains unknown. As a result, the slicing approach and atomic trajectory tracing approach (ATTA) were utilized to examine the void collapse behaviors.

In Figs. 2(I) and 2(II), two typical void collapse mechanisms—compressive collapse and spontaneous collapse—were presented through the slicing approach. Concretely, two voids named Void 1 for the small one and Void 2 for the big one appeared at $t = 37.0$ ps in Fig. 2(I). Another two voids enclosed by the red circle were also formed under the tensile stress at $t = 38.0$ ps. The further growth of these two voids resulted in the coalescence to generate a big void at $t = 44.0$ ps, and this big void finally coalesced with Void 2 at $t = 48.0$ ps. At $t = 40.0$ ps, the ligament between Voids 1 and 2 became shorter as they grew up. It was distinctly observed that Void 1 was compressed due to the outward expansion of Void 2 at $t = 44.0$ ps, which caused the edge of Void 1 close to Void 2 to begin to shrink inward. Accompanied by the further growth of Void 2 toward Void 1, Void 1 shrank quickly at $t = 48.0$ ps, eventually collapsing completely at $t = 50.0$ ps. Additionally, it should be highlighted that the ligament connecting Voids 1 and 2 was never severed during the whole collapse process.

Another important collapse process, spontaneous collapse, was discovered in the second spallation zone of the SC model. In Fig. 2(II), Void 3 was extremely close to a small void that was on the top of Void 3 at $t = 53.0$ ps, and two voids coalesced at $t = 53.6$ ps. Void 3 grew and became bigger at $t = 60.0$ ps, then started to shrink at $t = 70.0$ and 80.0 ps until collapsing altogether at $t = 90.0$ ps. Even though there were other large voids nearby, none had coalesced with Void 3, and there was no compression on it during their expansion processes. Consequently, spontaneous collapse was responsible for the collapse of Void 3.

The void collapse behavior was also discovered in NC Al, as illustrated in Fig. 2(III). First, Void 4 reached its biggest size from $t = 41.0$ to 44.0 ps. Then it commenced to shrink inward after $t = 50.0$ ps, continued to contract at $t = 60.0$ ps, until an approximate complete collapse at $t = 69.0$ ps. Similarly, some other larger voids were around Void 4, but none had merged with it. To further explore the evolutionary behavior of Void 4, the ATTA was used to examine its outward expansion or inward shrinkage. If the outer edge of the atomic trajectory was red, it indicated that the void expanded outward; conversely, if the outer edge was not red, it indicated that the void shrank inward and maybe even collapsed. In Fig. 2(III)(e), the atomic trajectory of Void 4 was clearly shown to expand outward at $t = 41.0-44.0$ ps. However, it displayed an inward shrinkage at $t = 44.0-50.0$ ps, suggesting that Void 4 had begun to collapse. Void 4 further shrank during $t = 44.0-69.0$ ps. Here, it should be noted that the void on the left side of Void 4 likewise expanded outward, which demonstrated that Void 4 was a compressive collapse. Furthermore, this collapse tendency was also confirmed by the last snapshot of the atomic trajectory.

Figure 2(IV) further illustrates the radius histories of Voids 1, 3, and 4. The equivalent radius r was calculated by the void volume formula based on the assumption that the void shape was ideally treated as a sphere [23]. The radius of Void 1 (blue void) initially increased and then decreased, which virtually reflected the void nucleation, growth, and collapse processes. A similar trend was also observed in Voids 3 and 4. All the curves mainly displayed three common traits. On the one hand, the growth velocity was larger than the collapse velocity, particularly for Voids 3 and 4; on the other hand, once the void reached its maximum size, the collapse would occur; however, this did not imply that the collapse would occur all the time, but rather that it would alternate with growth, like Voids 1 and 4. The last trait was that the collapse velocity was initially sluggish but quickly increased right before a total collapse. Additionally, the three-dimensional morphologies of Voids 1, 3, and 4 complementally confirmed the void collapse behaviors obtained from the slicing observation.

According to the Rayleigh-Plesset (R-P) equation, void nucleation, growth, and collapse are strongly associated with material strength, surface energy, inertial effect, and material viscosity effect [42]. The viscosity effect would not be highlighted in solid materials since it is always tied to void evolution in liquid metals. A void would nucleate when the dynamic tensile stress exceeded the nucleation threshold. The void size was extremely small after the void nucleation was just completed. Thus, the surface energy/tension largely hampered its growth. Meanwhile, the inertial effect initially also hindered the void growth. However, when compared with strong tensile stress, the surface tension and inertial effect became inappreciable, causing the void to grow quickly. According to the NAG theory, the void growth threshold was much smaller than the nucleation threshold [40]; therefore, tensile stress would drop rapidly once the void began to expand outward. As the void size further increased, the surface tension effect gradually became unobtrusive, while the inertial effect shifted from hindering to promoting void growth, namely, it started to predominate and accelerate the void growth, leading the void radius to promptly increase at an initial growth stage.

Even after the void reached its maximum size, the inertial effect continued to stimulate its expansion. After reaching its maximum size, the void began to collapse morphologically. Noting that the matrix bulk could hardly suffer the tensile stress due to the quasifractured spallation zone, see the atomic snapshot slices in Figs. 2(I)–2(III). It appeared improbable, therefore, that the tensile stress was mainly responsible for the secondary growth of the void. The secondary growth might be attributed to the thermal softening of the material around the void under lower tensile stresses and inertial effect. The local thermal accumulation resulted in material softening around the void due to an adiabatic shock, so the thermal softening could promote unstable growth. The void radius continued to shrink steadily as the inertial effect changed from promoting

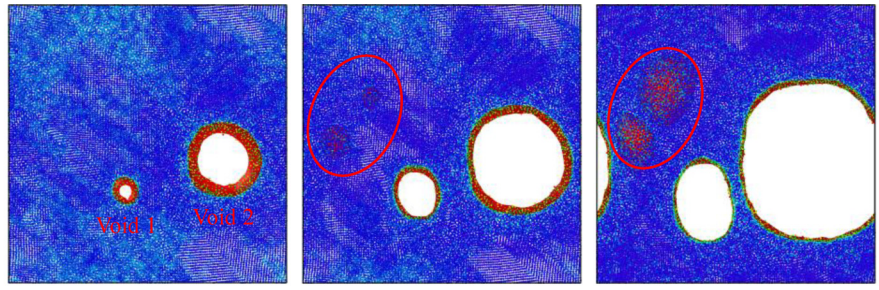

(a) $t = 37.0$ ps (b) $t = 38.0$ ps (c) $t = 40.0$ ps

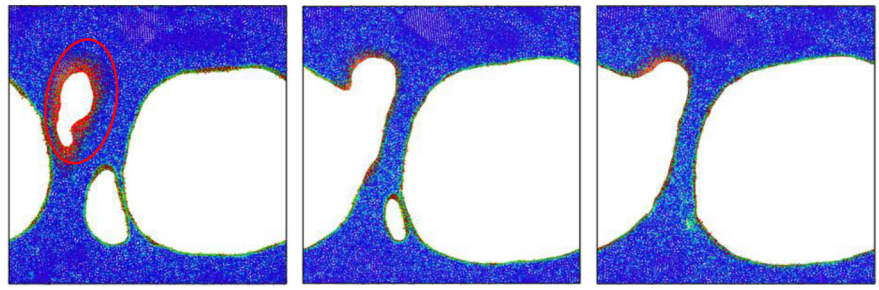

(d) $t = 44.0$ ps (e) $t = 48.0$ ps (f) $t = 50.0$ ps

(I) Void 1 evolution in the first spallation zone of the SC model

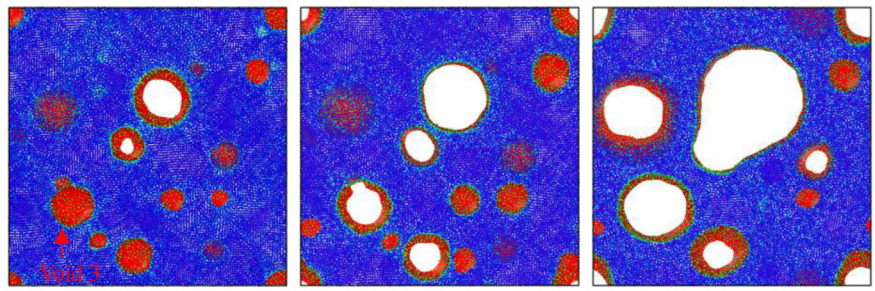

(a) $t = 53.0$ ps (b) $t = 53.6$ ps (c) $t = 60.0$ ps

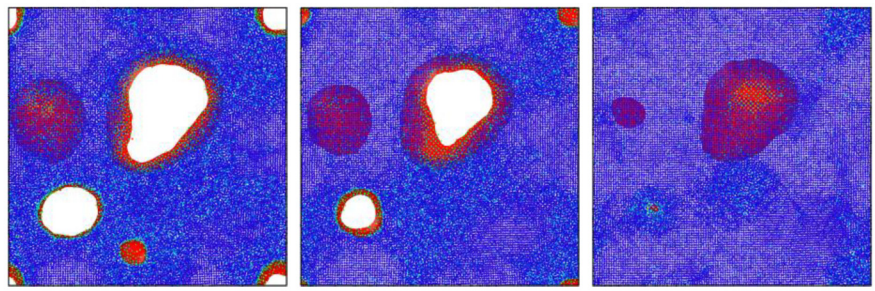

(d) $t = 70.0$ ps (e) $t = 80.0$ ps (f) $t = 90.0$ ps

(II) Void 3 evolution in the second spallation zone of the SC model

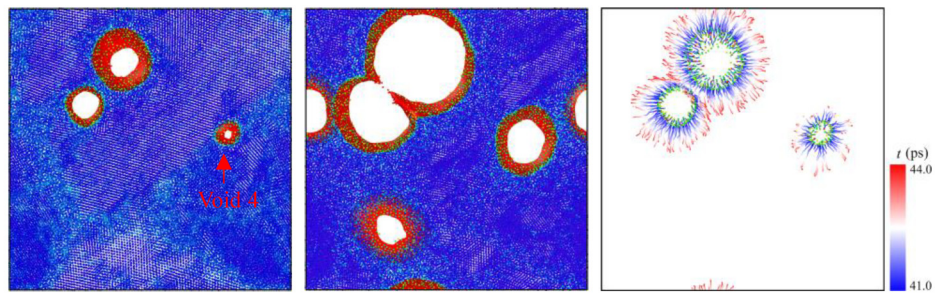

(a) $t = 41.0$ ps (b) $t = 44.0$ ps (e) $t = 41.0$-44.0 ps

FIG. 2. The full life cycle of the collapsed voids 1, 3, and 4 at $u_p = 1$ km/s, where the slicing is in the x-z plane, and its thickness is 2.0 nm.

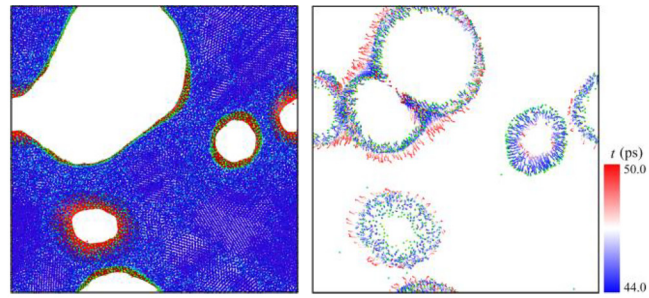

(c) $t = 50.0$ ps (f) $t = 44.0$-50.0 ps

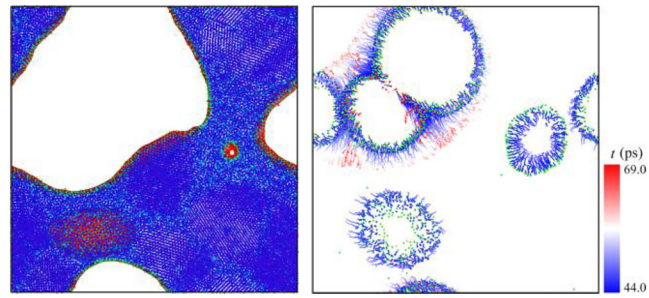

(d) $t = 69.0$ ps (g) $t = 44.0$-69.0 ps

(III) Void 4 evolution in the second spallation zone of the NC model, where (e)-(g) represent the atomic trajectories

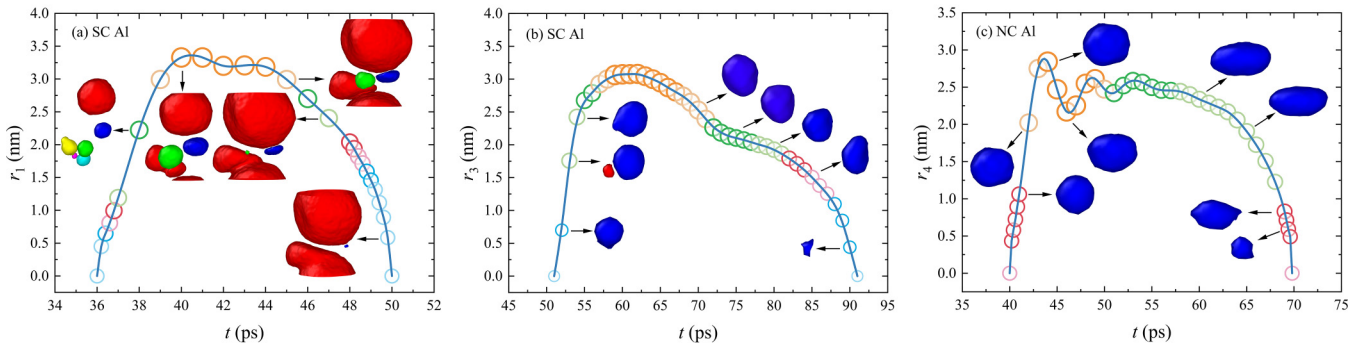

(IV) The variation in the equivalent radii of Voids 1, 3, and 4

FIG. 2. *(Continued.)*

to inhibiting void growth. When the radius was reduced to a particular value, surface tension became noticeable. Combined with a positive inertial effect on void collapse, the collapse velocity accelerated, causing a quick drop in void radius at the late stage of void collapse.

In Fig. 3, in the first spallation zone of the SC model at $u_p = 1$ km/s, it was evident that the spalled layer was not fully fractured; in the second spallation zone, the voids were not large enough to merge, and some of the smaller voids vanished as a result of the collapse at $t = 60.0-100.0$ ps. In the NC model, just one spallation zone at the free surface was formed, and it was partially detached from the matrix bulk. Additionally, at $t = 60.0-100.0$ ps, a few voids close to the loading end—that is, the left side of the snapshot—also collapsed. In contrast with the voids in the second spallation zone of the SC model, some of the voids were comparatively bigger, suggesting that the big void may collapse.

At $u_p = 2$ km/s, the spalled layer of the SC model started to separate from the matrix bulk under tensile stresses at $t = 30.0$ ps. At $t = 50.0$ ps, the entire separation between the spalled layer and matrix bulk formed. Some fragments, like spheres, were in the spallation zone, while other fragments, like cylinders, were still attached to the spallation fracture surfaces. At $t = 70.0$ ps, the cylinderlike fragments had all transformed into spherelike fragments, and as a result, the fracture surfaces became flat at $t = 70.0-100.0$ ps. Although there was just one spallation zone in the NC model, there were hardly any fragments, and the whole spallation fracture was not visible. The spalling evolutions at $u_p = 3-5$ km/s are additionally provided in Fig. S3 in the Supplemental Material [41].

Before analyzing the void data, some basic terms must be specified. For the sake of simplicity in calculating void volume, the void shape is considered spherical. The void volume V_v is calculated by

$$V_v = \sum_{i=1}^{N} \frac{4}{3}\pi r_i^3, \tag{1}$$

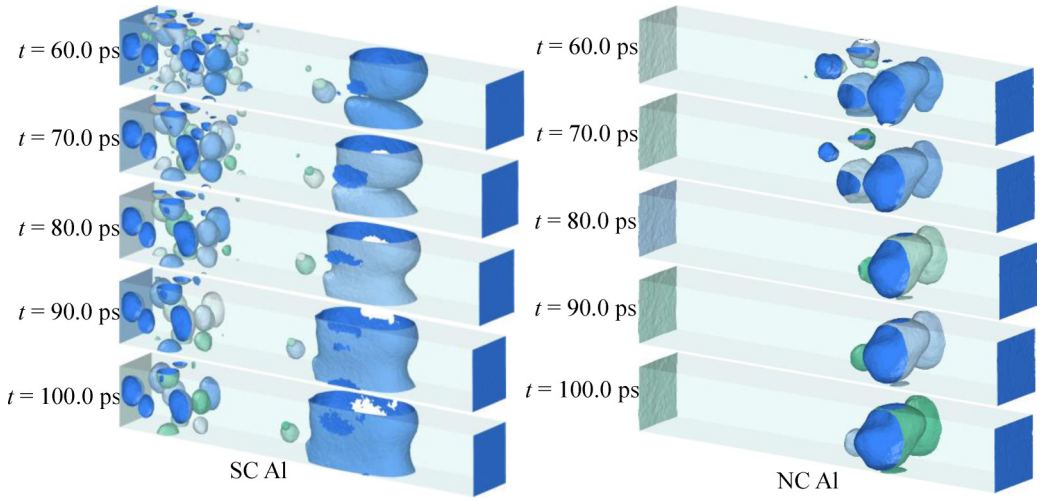

(a) $u_p = 1$ km/s

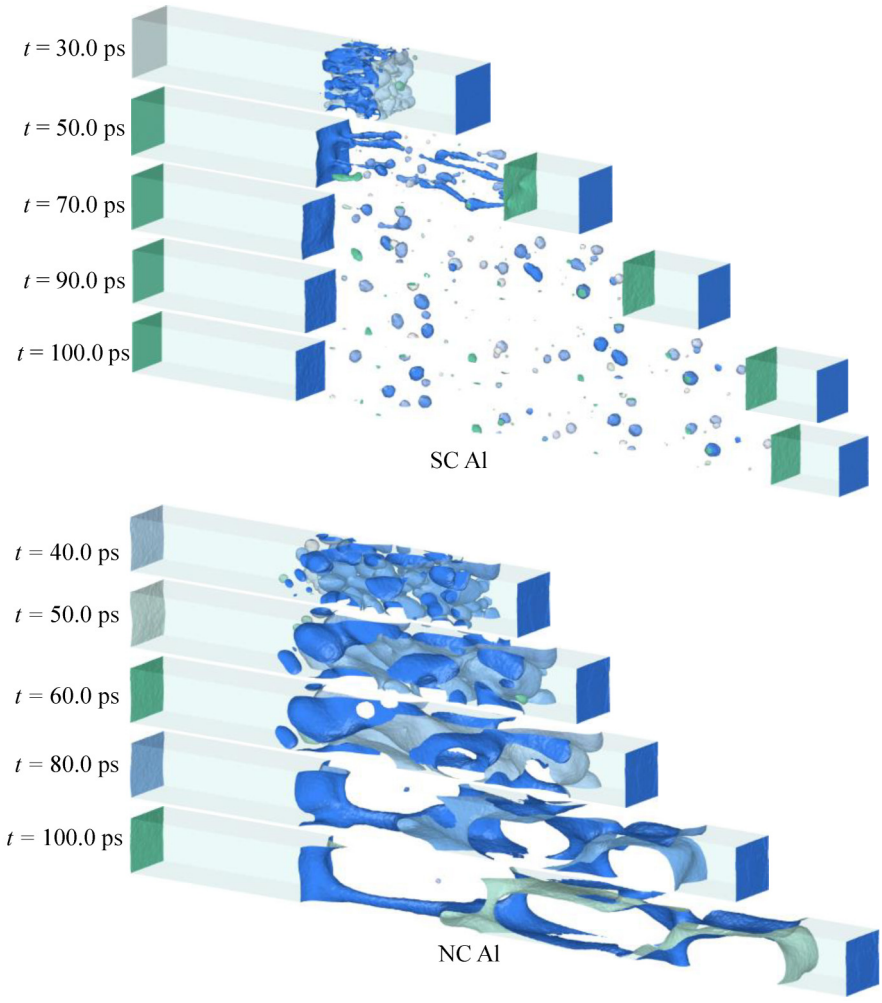

(b) $u_p = 2$ km/s

FIG. 3. Void evolution during the late stage of the spallation at $u_p = 1$ and 2 km/s.

where r_i is the radius of the ith void, $i = 1, 2, 3, \ldots, N$, where N is the current (or total) number of voids in the MD model.

The void volume fraction f_v is defined as

$$f_v = \frac{V_v}{V_s + V_v}, \tag{2}$$

where V_v and V_s are the void volume and the solid volume of the model, respectively.

In Fig. 4, at $u_p = 1$ km/s, void number N of the SC model increased first, then slightly fell due to the collapse and coalescence in the first spallation zone; next, the N largely increased

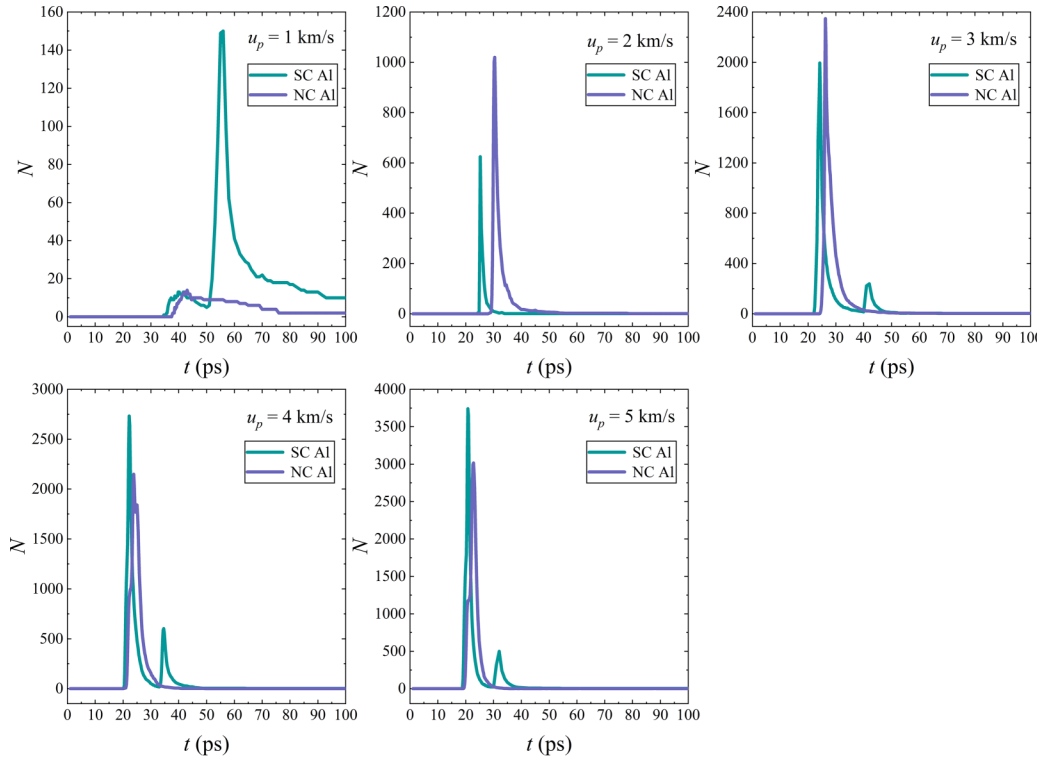

FIG. 4. The histories of void number N.

to the peak N_{max} due to the generation of the secondary spallation. After that, it first displayed a very quick drop and then a relatively slow drop and finally approached a constant. In the NC model, the N first rose and then slowly fell until it reached a constant value. Further, it should also be noted that the void maximum N_{max} of the NC model and the first peak of the SC model matched. The N of the SC and NC models initially soared and then quickly decreased, before reaching a constant at $u_p = 2$ km/s. In contrast with the NC model, N_{max} was substantially smaller in the SC model. The N histories of the SC models at $u_p = 3{-}5$ km/s shared the same change trend, with each curve exhibiting a secondary peak. However, because secondary spallation was absent in the NC models, there were no secondary peaks. The N_{max} in the NC model was higher than that in the SC model at $u_p =$ 3 km/s; inversely, N_{max} was larger in the SC model than in the NC model at $u_p = 4{-}5$ km/s. In addition, the histories of void radius r and void volume fraction f_v are shown in Fig. S4 in the Supplemental Material [41].

It should also be mentioned that the void number peak N_{max}, to some extent, reflected the ease and difficulty of void nucleation, namely, the larger the N_{max}, the easier the void nucleation and collapse. To be more specific, at $u_p = 1$ km/s, the N curves for the two models revealed a relatively mild rise before reaching the first peak, which indicated that the big voids might be generated, whereas the SC model had an intense increase before the secondary peak. At $u_p = 2{-}5$ km/s, it took very little time for N to erupt from nucleation to peak, suggesting that void nucleation occurred almost concurrently, irrespective of the spallation occurrence sequence. Next, it could be inferred that most of the voids were tiny in size at the void number peak, which implied that many of them would collapse, while the remaining voids would keep growing until they ultimately coalesced mutually, causing spallation. Consequently, to further grasp the information about void nucleation and collapse, the distribution of the void number N and void radius r at the peaks was examined in Fig. 5.

In Fig. 5(a), the voids in the two models were relatively less and varied in size in the snapshots, and the mild rise resulted in larger voids within a radius of 4–8 nm. This indicated that the void evolution should be nucleation, growth (i.e., the growth in both number and size), collapse, and coalescence. However, at $u_p = 2{-}5$ km/s, the voids were much more and relatively uniform in size. The intense increase led to smaller voids mainly within a radius of 0–2 nm, with the voids within 0–1 nm accounting for the overwhelming ratio, as shown in Figs. 5(b)–5(e). Overall, the void evolution should be nucleation, initial growth in number, collapse, late growth in size, and coalescence. Regarding the voids at the second peak, likewise, most of the voids were within 0–2 nm in Figs. 5(f)–5(i). At $u_p = 1$ km/s, the big void in the first spallation zone marked by the black frame exceeded 10 nm, as shown in the inset of Fig. 5(f); additionally, the larger voids within 2–5 nm were relatively more compared with the other cases at $u_p = 2{-}5$ km/s. Thus, it could be speculated that the voids in both spallation zones evolved in the same way under the same shock velocity.

B. Coupling behaviors of spallation and microjetting

In Fig. 6, at $u_p = 1$ km/s, no jet appeared in the SC and NC models, and the sinusoidal perturbation almost remained its original shape due to the low shock pressure. The SC microjetting model, like the SC spallation model, also formed two

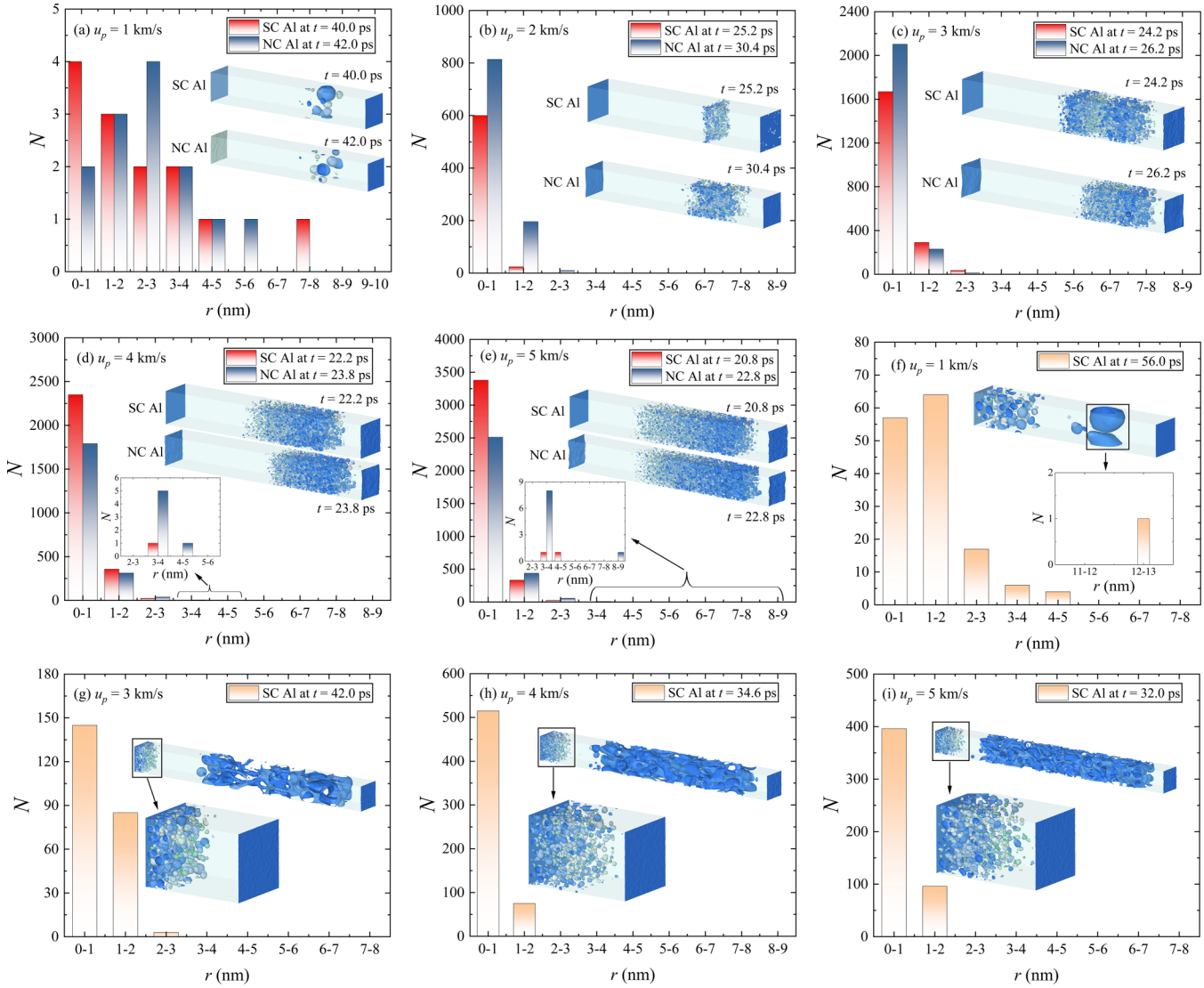

FIG. 5. The distribution statistics between void number N vs its radius r at the wave peaks of the N histories, where (a)–(e) and (f)–(i), respectively, denote the void distribution statistics at the first and second peaks, in which (f) denotes the void distribution statistics in both two spallation zones, and (g)–(i) denote void distribution statistics only in the secondary spallation zone.

spallation zones, but only one spallation zone was generated in the NC microjetting model. At $u_p = 2$ km/s, it was clear that the two plane jets appeared before the voids in the SC microjetting model at $t = 24.2$ ps, but the void nucleation zone was extremely concentrated, which was very similar to the SC spallation model. The void number became more at $t = 25.0$ ps relative to multiple tiny voids at $t = 24.2$ ps, although the velocity of microjet development was very sluggish. Nevertheless, the NC microjetting model failed to generate jets due to the energy dissipation at the grain boundaries; instead, the atoms filled the perturbation troughs, nearly transforming it into a comparatively level free surface in contrast with the sinusoidal one. Additionally, the initial evolutions of spallation and microjetting at $u_p = 3-5$ km/s are given in Fig. S5 in the Supplemental Material [41].

In terms of interior void evolution, however, the microjetting models exhibited a wider dispersion from the sinusoidal perturbation surface to the loading end than the spallation models. In short, there were no essential differences in the void evolution in spallation and microjetting models; however, the initial perturbation affected the void distribution, particularly at higher shock velocity.

In Fig. 7, the void evolution in both SC spallation and SC microjetting models was strikingly comparable at $u_p = 1$ km/s, particularly in terms of secondary spallation and the emergence of a medium void near the first spallation zone, as shown in Figs. 3(a) and 7(a). Additionally, it was readily apparent that the voids to the left of the initial spallation zone exhibited collapse behaviors in the NC models. At $u_p = 2$ km/s, two SC models were stretched under tensile stress at $t = 30.0$ ps, and the remarkable phenomenon was the formation of a microjet in the microjetting model. However, the microjet totally disappeared at $t = 100.0$ ps. The free surface had been changed from a sinusoidal perturbation to

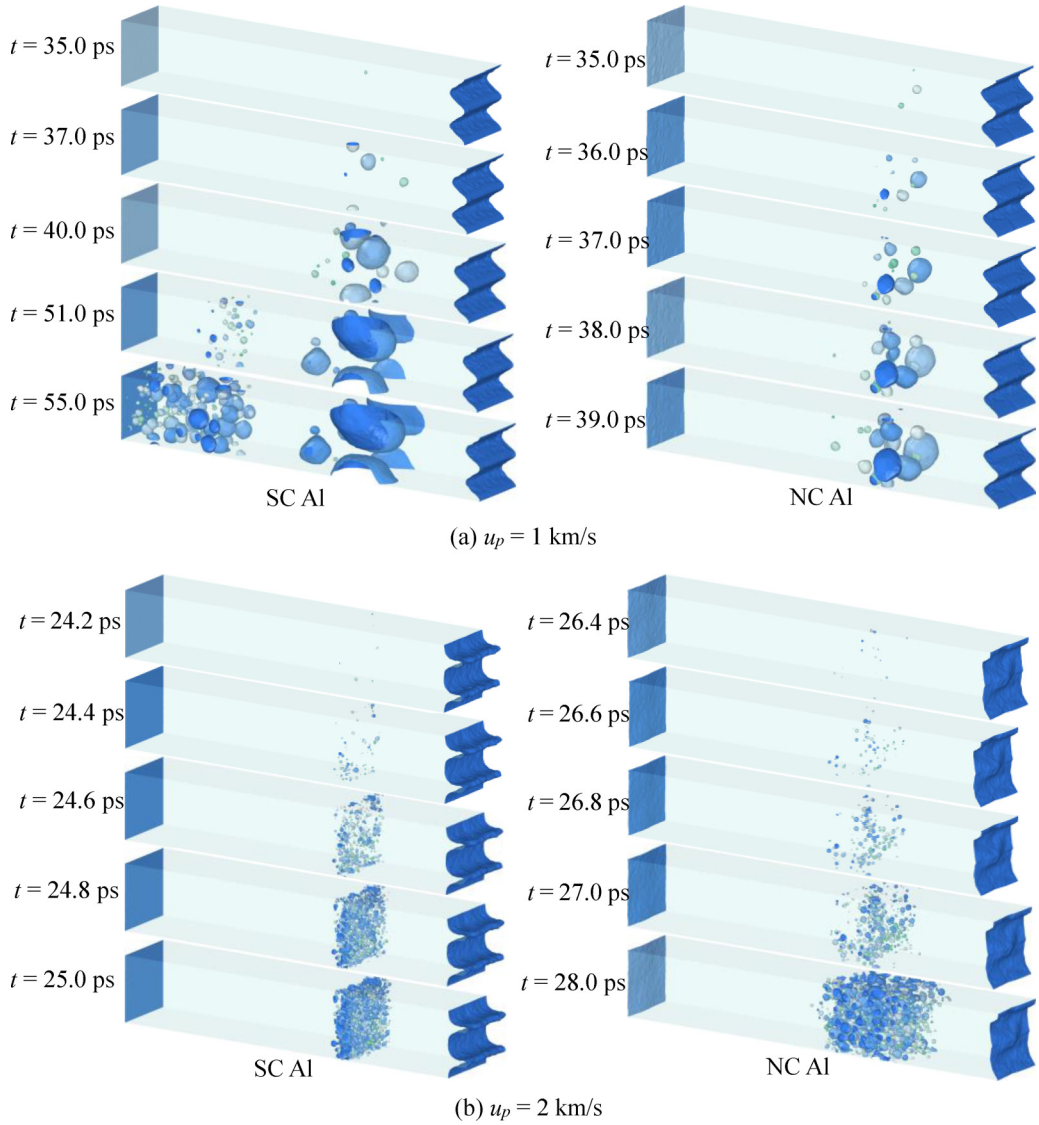

FIG. 6. The initial evolutions of spallation and microjetting at $u_p = 1 - 2$ km/s.

a flat surface in the microjetting model, which was the same as the free surface of the spallation model. Additionally, the spallation fracture surfaces also evolved into smooth surfaces in both models. In the NC microjetting model, the sinusoidal perturbation developed into an uneven surface rather than a flat one due to no formation of a microjet; in two NC models, the spalled layer remained incompletely fractured, resulting in nonflat spallation fracture surfaces.

Combined with the cases at $u_p = 3-5$ km/s, shown in Fig. S6 in the Supplemental Material [41], the disappearance and total fragmentation of the jet are two basic approaches for flattening the free surface. Another approach is maintaining phase noninversion while filling the trough, shown in the NC model at $u_p = 2$ km/s.

In the microjetting models, we also performed the statistics on the void number N, see Fig. 8; and the void radius and void volume fraction are additionally provided in Fig. S7 in the Supplemental Material [41]. It was found that the magnitudes and tendencies of change for N were strikingly like the spallation models in Fig. 4.

Nevertheless, certain minor differences remained, such as the void maximum, as listed in Table II. Regardless of the free surface type, just one spallation zone was generated in all the NC models, and the SC models also showed an analogous occurrence at $u_p = 2$ km/s. In the SC and NC models, $N_{\max 1}$ essentially rose as u_p increased, but $N_{\max 2}$ reached its maximum at $u_p = 4$ km/s and subsequently decreased at $u_p = 5$ km/s, and it was slightly larger in the microjetting model than in the spallation model.

As of now, only a fundamental comprehension of the coupling behaviors of spallation and microjetting remain. Thus, to obtain an in-depth understanding of the microjet behaviors in the SC and NC models, three typical cases are provided in Fig. 9.

In Fig. 9(a), upon reaching the wave trough, the shock wave underwent reflection, and the rarefaction wave caused the

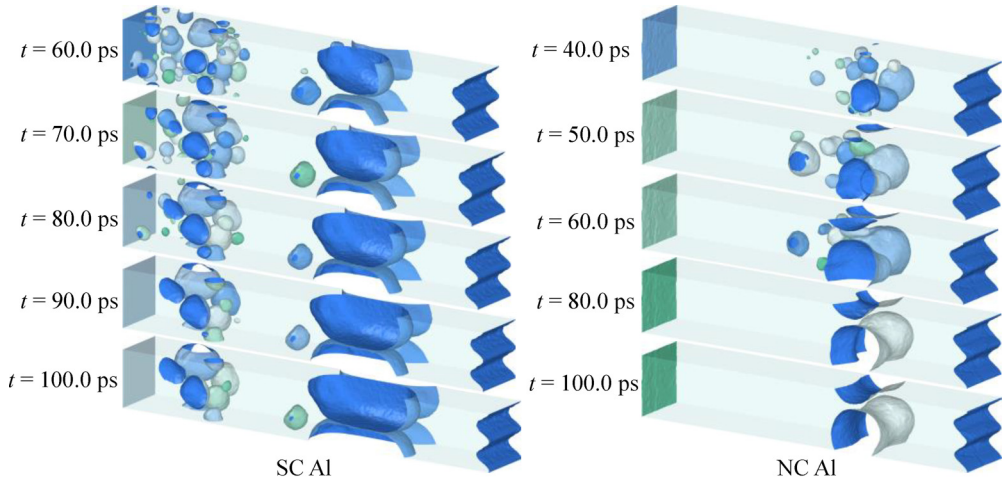

(a) $u_p = 1$ km/s

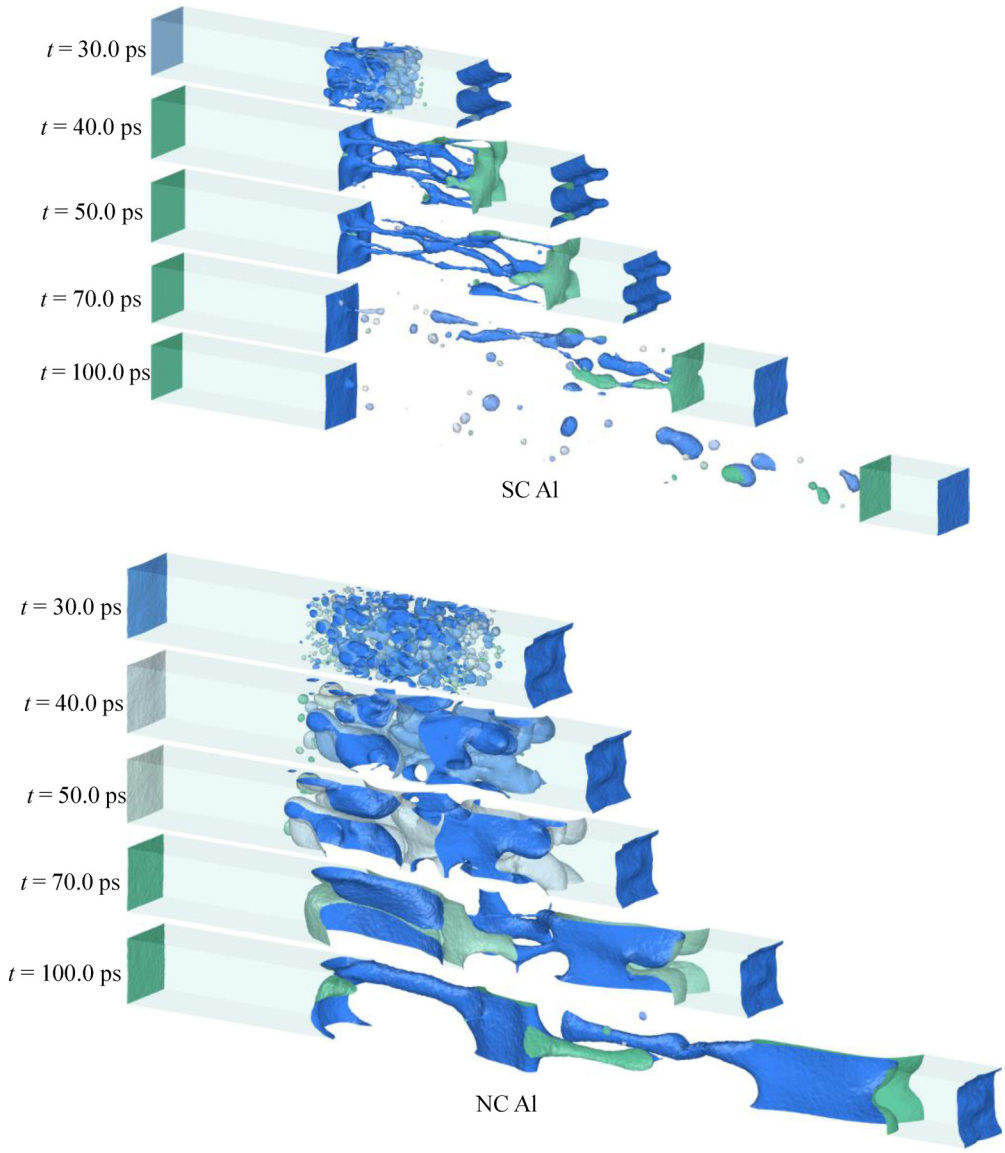

(b) $u_p = 2$ km/s

FIG. 7. The late evolutions of spallation and microjetting at $u_p = 1$ and 2 km/s.

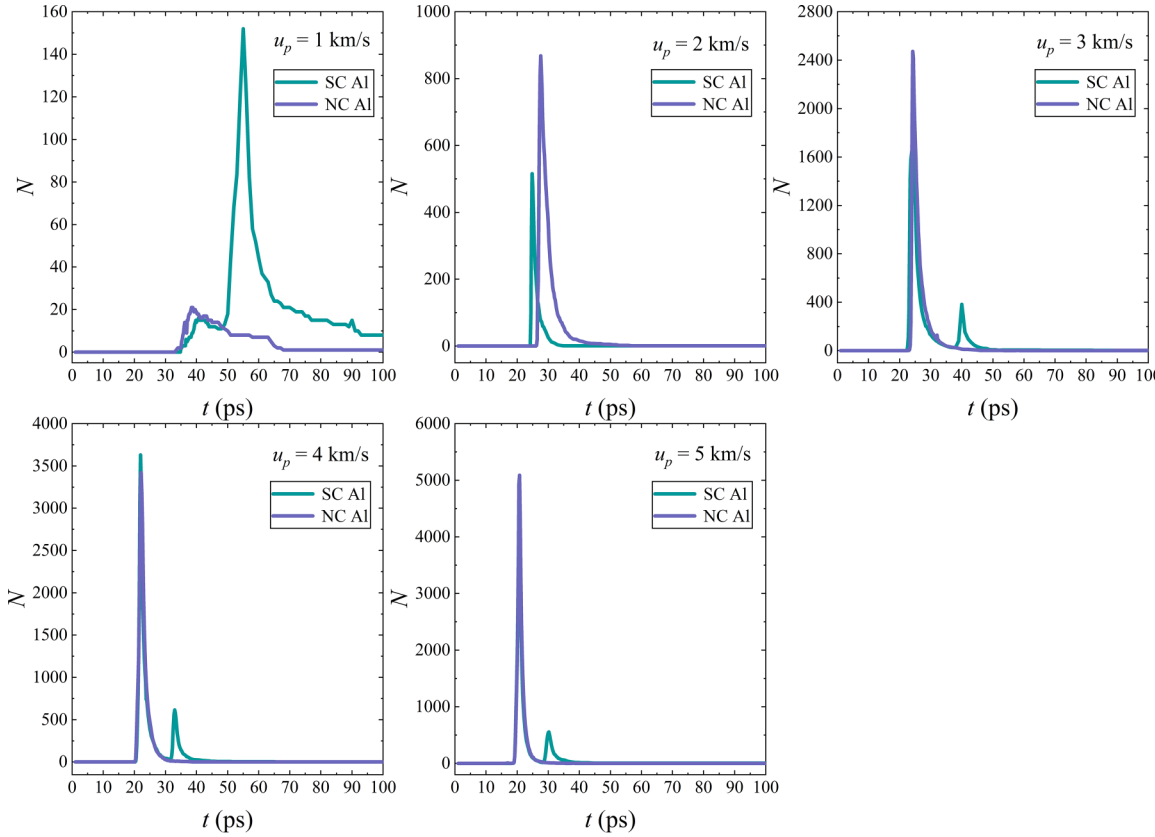

FIG. 8. The histories of void number N.

atoms located in the perturbation trough to initiate movement along the shock direction at $t = 18.0$ ps. With the stress wave propagating to the perturbation peak, the atoms at both sides of the wave trough started to converge to form the rudimentary jets at $t = 19.0$ ps. Concurrently, the original perturbation virtually vanished. When the stress wave reached the perturbation peak, all the atoms in the vicinity of the perturbated free surface would be ejected into the Y direction, causing a further development of the jets at $t = 20.0$ ps. When the jets were in a phase inversion state, a spike and bubble were formally generated at $t = 30.0$ ps. After $t = 40.0$ ps, the spike heads got thicker, and the spike length became shorter at $t = 45.0$ and 50.0 ps. At $t = 55.0$ ps, the original sinusoidal perturbation reverted to a phase inversion one due to a further decrease in jet length. The jet completely disappeared, and the perturbated surface became flat at $t = 60.0$ ps, phenomenologically demonstrating that the microjet had degenerated into spallation.

In Fig. 9(b), the NC model, like the SC model at $u_p =$ 2 km/s, exhibited a similar forming process at $u_p = 3$ km/s, although with longer and thicker spikes, as shown in the snapshots at $t = 15.2-20.0$ ps. Two spikes became uneven in length, and the left one (i.e., the lower jet in the oblique snapshot) was longer than the right one (i.e., the upper jet in the oblique snapshot) at $t = 40.0$ ps. Here, it was observed that the left spike diverged from the original path along the Y direction. In comparison with the jets at $t = 40.0$ ps, the body of the spike became thinner, but it did not show any voids at $t = 70.0$ ps. It could be inferred that the jet kept growing without any breakage at $t = 40.0-70.0$ ps. The atoms at the body of the spike piled up close to its head because of the velocity gradient, making the head thicker. Otherwise, the

TABLE II. The $N_{\max}$ comparison between spallation and microjetting models.[a]

		$u_p = 1$ km/s		$u_p = 2$ km/s		$u_p = 3$ km/s		$u_p = 4$ km/s		$u_p = 5$ km/s	
Model	Material type	$N_{\max 1}$	$N_{\max 2}$	$N_{\max 1}$	$N_{\max 2}$	$N_{\max 1}$	$N_{\max 2}$	$N_{\max 1}$	$N_{\max 2}$	$N_{\max 1}$	$N_{\max 2}$
Spallation	SC	13	150	625	–	1996	239	2733	602	3741	499
	NC	13	–	1020	–	2347	–	2149	–	3016	–
Microjetting	SC	16	152	516	–	1691	383	3631	616	4509	556
	NC	21	–	868	–	2473	–	3420	–	5089	–

[a]$N_{\max 1}$ and $N_{\max 2}$ are the void maxima in the first and second spallation zones, respectively.

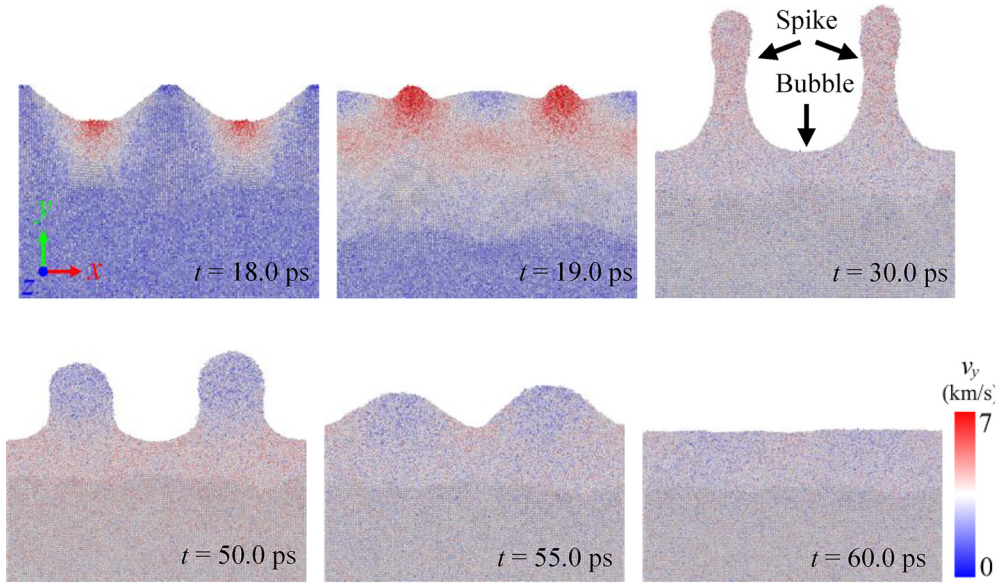

(a) SC Al at $u_p = 2$ km/s

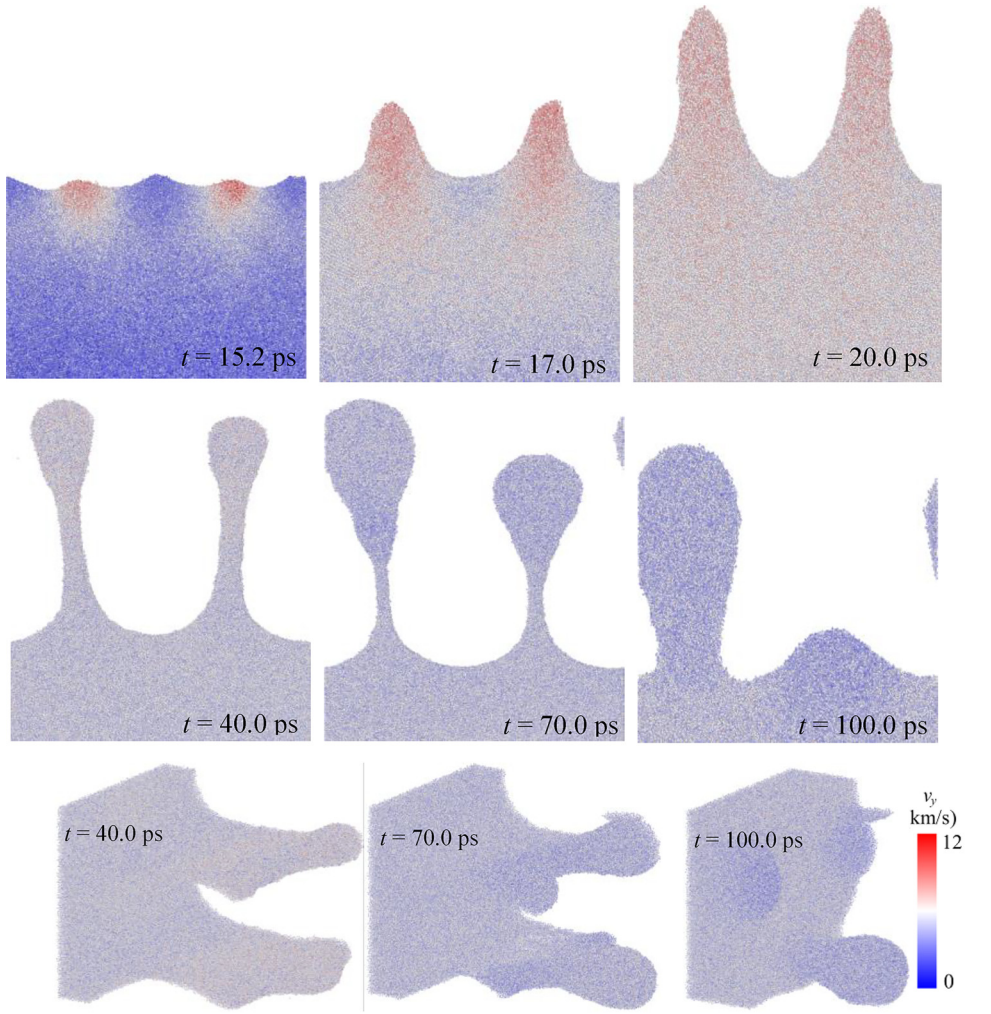

(b) NC Al at $u_p = 3$ km/s, where the snapshots at $t = 40.0$-100.0 ps were also displayed in an oblique view

FIG. 9. The typical evolutionary characteristics of the microjet.

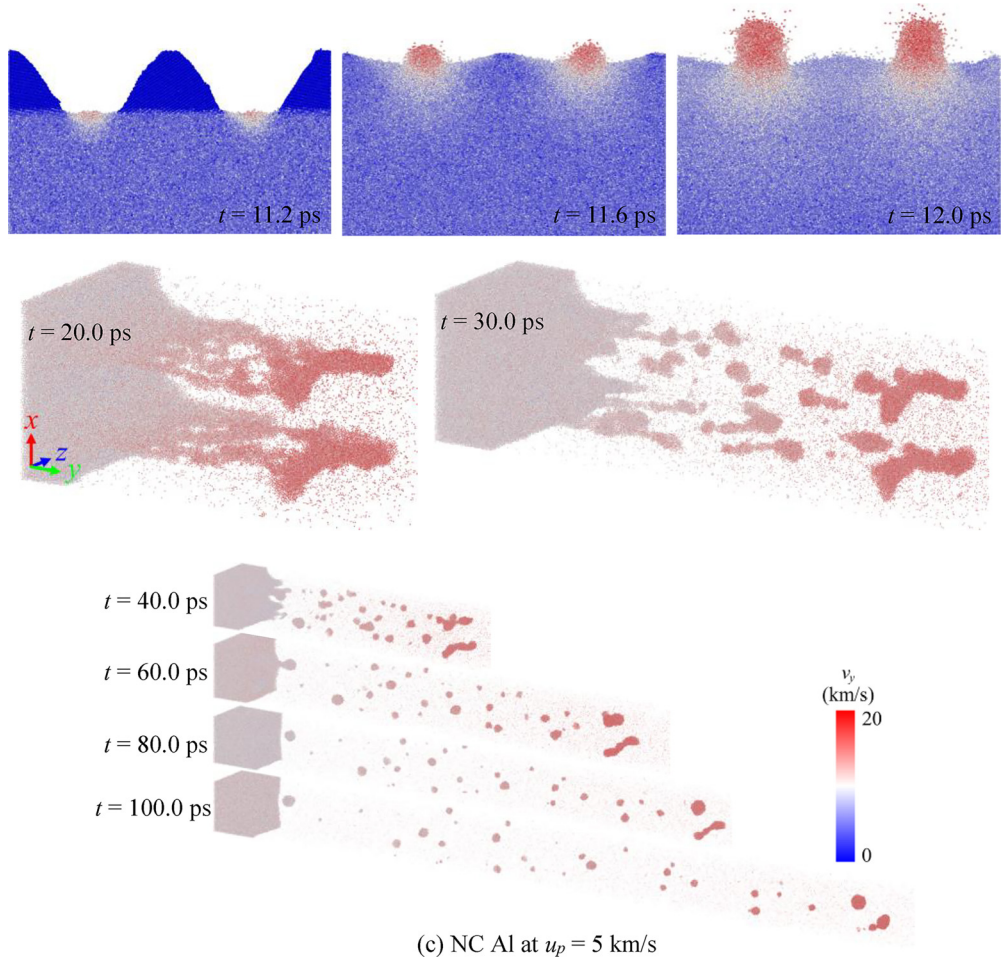

(c) NC Al at $u_p = 5$ km/s

FIG. 9. *(Continued.)*

left spike was shorter than the right one, suggesting that the former had been repressed. At $t = 100.0$ ps, the left spike got shorter and thicker as well as shrinking from a sheet to a stick, whereas the right spike nearly vanished.

In relation to the cases at $u_p = 2$ and 3 km/s, the generation process of the microjet at $u_p = 5$ km/s was quite comparable. However, the microjet was liquid due to the melting and numerous single atoms near the jet head detached from the jet at $t = 12.0$ ps in Fig. 9(c), forming the particle clouds. As the jets further developed, two jet sheets were broken at $t = 20.0$ ps, showing the instability of the jet. Then the broken sheets disintegrated into fragments at $t = 30.0$ ps. During $t = 40.0-100.0$ ps, the single irregular fragments were gradually transformed into spherelike ones due to the surface tension. The disintegration began in the middle parts of the sheet and respectively progressed to its tail and head. The breakup of the tail produced a flat surface, while the breakup of the crooked sticklike jet head resulted in bigger fragments than others.

In terms of the overall evolution of the microjet, two representative features were manifested here. The first described the formation, growth, arrest, and disappearance of the microjet, as shown in Figs. 9(a) and 9(b). Despite the lack of complete integration between the jet and spalled layers at $u_p = 3$ km/s in the NC model, it was hypothesized that a phenomenon resembling the SC case at $u_p = 2$ km/s would materialize given an adequate simulation duration. The second described the identical occurrences but included disintegration instead of disappearance, as seen in Fig. 9(c).

In fact, the microjet demonstrated a comparable forming mechanism; the difference was in its evolution. To facilitate the description, two phenomena mentioned above would be designated with nomenclatures. The models showed synchronized behaviors of the microjet and spallation throughout the evolutionary process. For the former, it was specifically referred to as degenerated spallation due to the disappearance of the microjets. Without considering the ejected fragments, the latter converted into microspallation; the coexistence of spallation and jetting behaviors is known as the spallation-jet coupling.

Determining the source of ejecta is crucial during the jet formation process. By using the particle tracing approaches, it was revealed that the jet formation was a layered aggregation process from the surficial layer of the defect to its inner layer based on the MD and Eulerian peridynamics methods in earlier work [26,31]. Thus, the ejecta source has not been described in detailed here. To quantitatively describe the jet growth and arrest behaviors, the spike length ξ was defined as

$$\xi = y_{sp} - y_b, \tag{3}$$

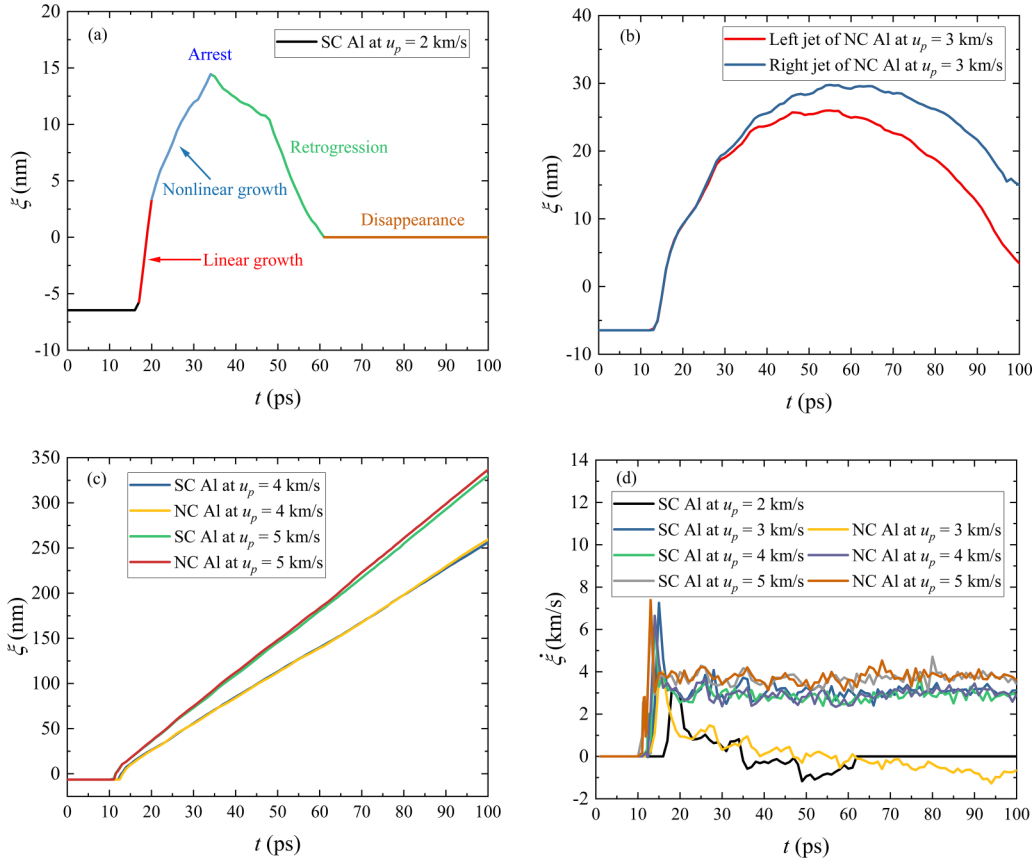

FIG. 10. The evolutions of (a)–(c) spike length ξ and (d) its velocity $\dot{\xi}$.

where y_{sp} and y_b are tip positions of the spike and bubble in the Y direction, respectively. Correspondingly, the relative velocity between the spike and bubble was

$$\dot{\xi} = \dot{y}_{sp} - \dot{y}_b = v_{sp} - v_b, \tag{4}$$

where the dot above the physical quantity represents the derivate with respective to time, and

$$v_{sp} = \frac{y_n - y_{n-1}}{\Delta t}, \tag{5}$$

where y_n and y_{n-1} represent the position along the Y direction of the spike tip at successive time steps n and $n-1$, and Δt represents the time internal between y_n and y_{n-1}.

In Fig. 10, the spike length ξ of SC Al at $u_p = 2$ km/s rose linearly at first and then nonlinearly. Following that, it reached its peak at $t = 34.0$ ps, showing the spike growth arrest and a critical transition from increase to decrease. Subsequently, it began to fall, demonstrating its fading, and ultimately approached zero, suggesting its disappearance. The left and right spike lengths in the NC model varied similarly at $u_p = 3$ km/s, but at $t = 30.0$ ps, they began to diverge, with the right spike being bigger than the left. This might be caused by the grain boundary effect. Furthermore, it did not exhibit spike extinction at $t = 100.0$ ps, in contrast with the situation in SC Al at $u_p = 2$ km/s. At $u_p = 4$ and 5 km/s, the spike length increased linearly, and the length evolution revealed no difference between SC and NC models at the same shock velocity. In Fig. 10(d), all the relative velocity curves proliferated at first, with the difference being the drop variation. The curves at $u_p = 2$ and 3 km/s steadily decreased and ultimately became negative, indicating that the spike length began to decrease. When the velocity was reduced to zero, the spike vanished, and the free surface became flat. Other curves would be somewhat fluctuating around a constant. The variations in the spike length and its velocity were also discovered to be similar in the SC Sn model [43].

Further, the spike tip velocity v_{sp} was also presented in Fig. 11. The v_{sp} curve at $u_p = 2$ km/s first soared to the peak before rapidly declining until it reached zero, as shown in Fig. 11(a). In Fig. 11(b), the v_{sp} curves likewise surged initially before swiftly dropping to a constant. The NC and SC models eventually neared the same constant, despite the peak of the NC model being bigger. The v_{sp} curves in the NC models at $u_p = 4$ and 5 km/s showed a similar variation to the curve at $u_p = 3$ km/s. While for the SC model the v_{sp} curve at $u_p = 4$ km/s displayed a minor drop after reaching its maximum value and then approached a constant, the v_{sp} curve at $u_p = 5$ km/s approached the constant rather than descending. It was observed that the peak of the NC model was higher than that of the SC model, particularly in the cases at $u_p = 4$ and 5 km/s, where it was about twice as high. To begin with, it should be made clear that the maximum velocity of the spike tip emerged at an early stage of its formation. Naturally, the particles on the outermost surface of the perturbation valley were the first to be ejected due to the reflection of the compressive wave, resulting in the formation of the jet tip with the maximum kinetic energy. The grain boundary, as a defect in the NC model, made the material discontinuous

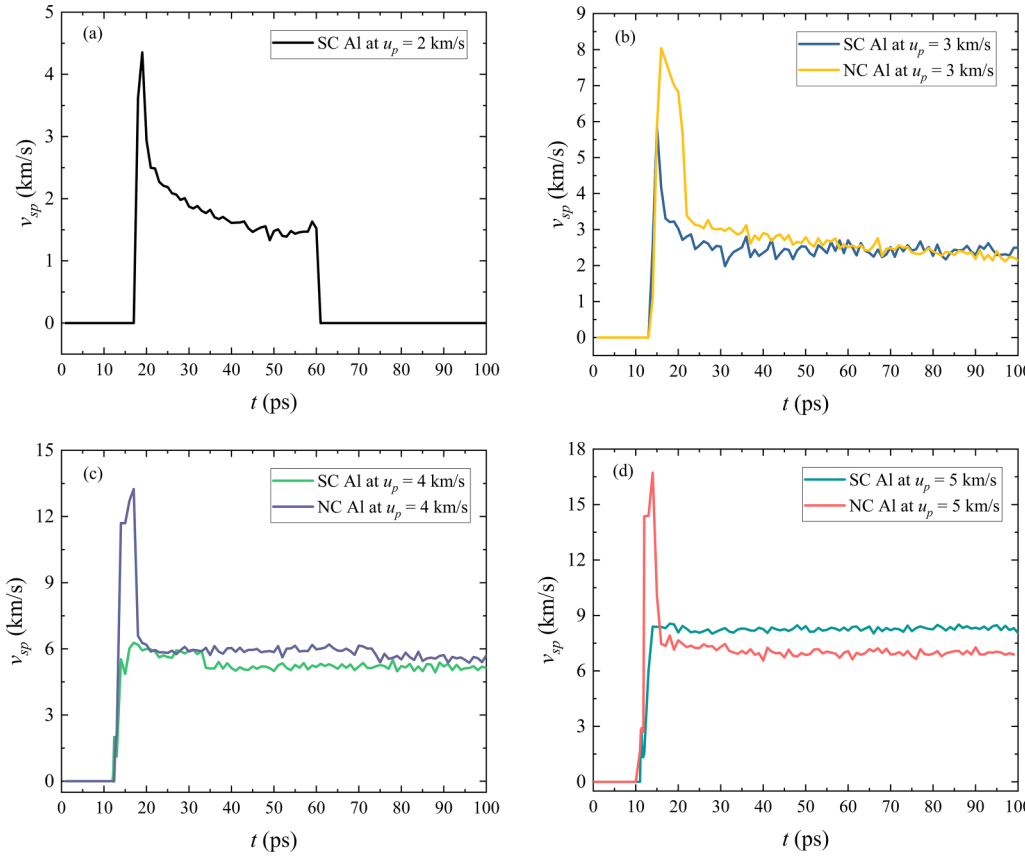

FIG. 11. Spike tip velocity v_{sp} evolution.

when compared with the SC material. This discontinuity in the physical property induced inhomogeneous deformation, leading to the velocity difference in the sheet tip, which was particularly reflected in jet evolution at the late stage, as shown in Fig. 9(b). Thus, a higher velocity of the spike tip in the NC model might be attributed to the inhomogeneous deformation.

Once the jet sheet entered unstable growth, it was more likely to break. During the process of unstable growth to fragmentation, the formation and evolution of the fragment had an important influence on the distributions of the size, volume, mass, etc. Therefore, understanding the fragmentation mechanisms is critical to fragment distribution laws.

Figure 12 illustrated three important fragmentation mechanisms of the jet sheet. The sheet got thinner in the body and thicker in the head as it expanded in the shock direction. When the sheet reached a critical thickness, some tiny voids appeared at $t = 20.0$ ps in Fig. 12(a). The void nucleation could not be effectively recognized due to the amorphous structure of the sheet. The snapshots at $t = 22.0-30.0$ ps thoroughly show the broken process caused by the void growth and coalescence, which demonstrates the same micromechanism as the ductile spallation behavior. Furthermore, the head of the sheet changed into a crooked stick, and the crooked position was connected to the ligament, preventing its mobility. It could be inferred that the nucleation, growth, and coalescence of the void were the primary cause of the plane jet fragmentation.

Another critical reason for jet fragmentation was caused by tensile stress, as seen in Fig. 12(b). Specifically, the residual columnar fragmentation often appeared after the jet sheet was broken, namely, the plane jet was changed into a one-dimensional jet, see the snapshots at $t = 50.0$ and 55.0 ps. Because the necking was visible in this columnar jet, its head was on the brink of breakage at $t = 60.0$ ps; the jet had been pinched off shortly after 10 ps, indicating jet breakup. It should be noted that the void also collapsed during $t = 50.0-60.0$ ps. Thereafter, the head fragment shaping process progressed from irregular to spherical, and the position where the jet was pinched off got thicker at $t = 80.0$ ps. The repeated fragmentation behavior appeared at $t = 90.0-100.0$ ps.

Phenomenologically, the necking triggered jet breakup. In fact, jet breakup was precipitated by temperature, velocity, and stress perturbations. Two adjacent segments being broken presented comparable temperatures, which did not produce a temperature gradient, so the temperature perturbation was not mainly responsible for the breakup. In our previous study [26], we discovered that the velocity gradient had the largest influence on jet breakup. Note that the velocity gradient was the root source of tensile stress during the jet evolution. The breakup behavior of a one-dimensional jet appeared to be driven by a velocity gradient, but it was produced by tensile stress along the shock direction. Thus, the longitudinal tensile stress generated the necking or pinch-off behavior in the jet development, which was quite comparable with the

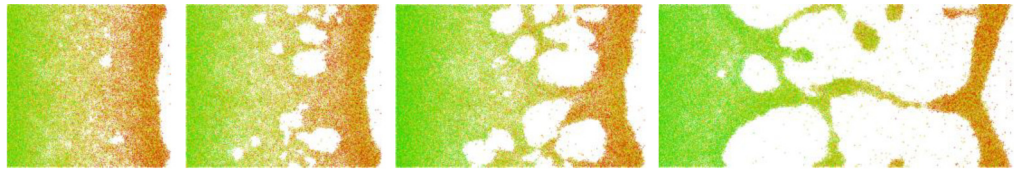

$t = 20.0$ ps $t = 22.0$ ps $t = 24.0$ ps $t = 30.0$ ps

(a) Fragmentation mechanism I: void nucleation, growth, and coalescence

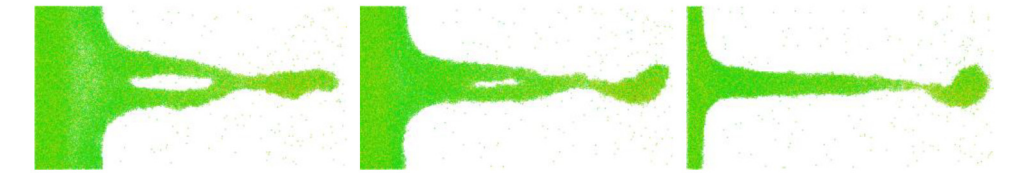

$t = 50.0$ ps $t = 55.0$ ps $t = 60.0$ ps

$t = 70.0$ ps $t = 80.0$ ps $t = 90.0$ ps $t = 100.0$ ps

(b) Fragmentation mechanism II: longitudinal necking induced by the tensile stress

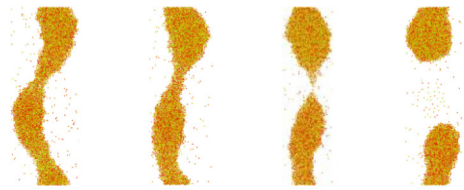

$t = 40.0$ ps $t = 50.0$ ps $t = 60.0$ ps $t = 70.0$ ps

(c) Fragmentation mechanism III: transverse necking induced by the shear and tensile stresses

FIG. 12. Fragmentation mechanisms of the jet sheet, where the sheet, coming from the nanocrystalline (NC) model at $u_p = 4$ km/s, was the left one; all the snapshots were in the y-z plane.

macronecking phenomena of ductile metal under the uniaxial tensile test.

Additionally, the breakup of the jet head is also presented in Fig. 12(c). At $t = 40.0$ ps, a necking phenomenon is shown in the middle of the crooked head. At $t = 50.0$ ps, the radius of the necking zone became smaller, and the two ends of the necking zone got bigger, suggesting that the tensile stress was perpendicular to the shock direction. This was referred to as *transverse tensile stress*. At $t = 60.0$ ps, the crooked head was pinched off at the necking zone by the transverse tensile stress. Also, it should be observed that, after the lower fragment had caught up with the upper one, these two fragments were roughly parallel in the shock direction. Due to the relative movement of two fragments in the shock direction, the shear stress would be generated at the necking zone during the catch-up process; correspondingly, the shear stress direction was basically along the shock direction. Therefore, the jet head breakup could be attributed to the transverse tensile and shear stresses.

It could be seen that the fragmentation mechanism of plane jet was exceedingly sophisticated. First, due to void nucleation, growth, and coalescence, the plane jet evolved into fragments and one-dimensional jets, with the latter including the residual columnar jet attached to the free surface and the jet head. The longitudinal tensile stress was then responsible for the columnar jet breakup, while transverse tensile stress and shear stress contributed to the jet head breakup.

The disintegrated jet eventually evolved into fragments. Thus, the following research will focus on fragment size distribution and evolution throughout the fragmentation process.

Figure 13 showed a typical example of fragment evolution, and other cases for SC and NC models at $u_p = 4$ and 5 km/s can be found in Fig. S8 in the Supplemental Material [41]. In Fig. 13, most of the fragments are in the range of $0-10\,\mathrm{nm}^3$ at $t = 30.0$ ps. As the jet broke up, the fragments of $20-30\,\mathrm{nm}^3$ increased at $t = 40.0$ ps. At $t = 50.0-100.0$ ps, the fragments of $50-100\,\mathrm{nm}^3$ likewise emerged, whereas the fragments of $0-10\,\mathrm{nm}^3$ virtually remained unchanged. It should also be mentioned that the jet head was represented by fragments $>100\,\mathrm{nm}^3$. The fragment number N_f of $0-10\,\mathrm{nm}^3$ is comparable in the SC models at $u_p = 3$ and 4 km/s, and for the latter, nearly all the fragments were

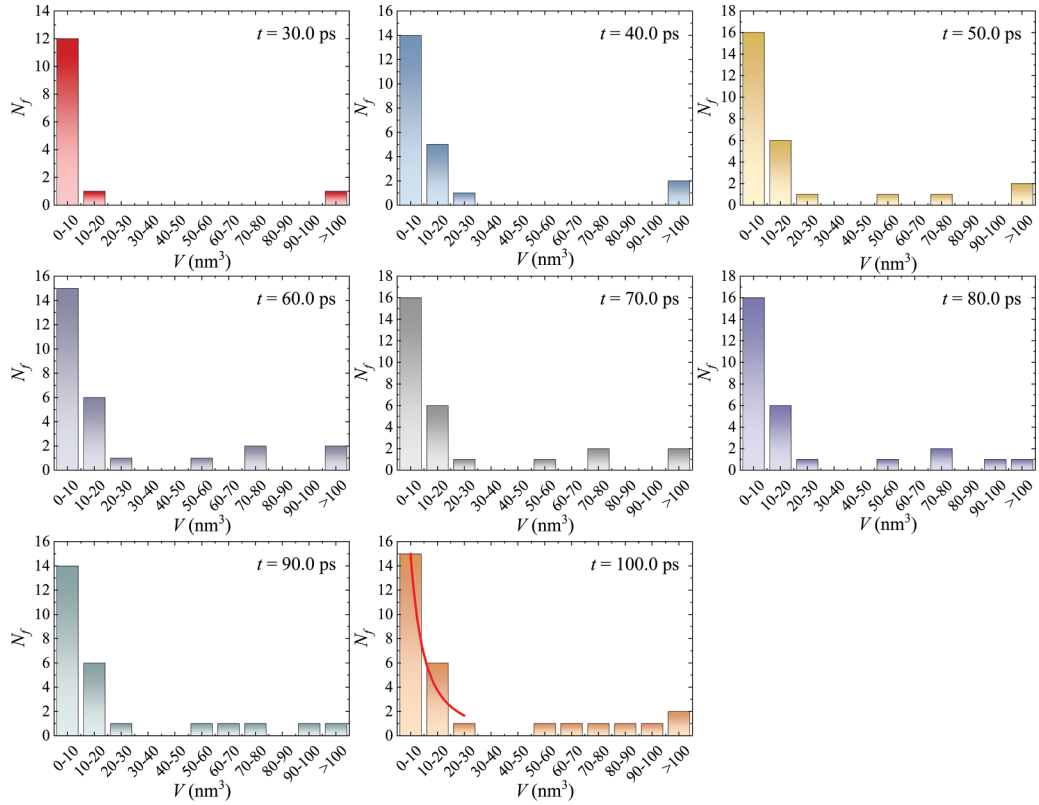

FIG. 13. Volume V vs number N_f distribution of the fragment in single-crystal (SC) Al at $u_p = 3$ km/s.

within the range of $0-30\,\mathrm{nm}^3$. However, compared with the SC model, the N_f became less in the NC model at $u_p = 4$ km/s; the fragments predominantly fell into the range of $0-50\,\mathrm{nm}^3$, the fragments within $50-90\,\mathrm{nm}^3$ were lacking, and the fragments $>90\,\mathrm{nm}^3$ slightly increased. At $u_p = 5$ km/s, the higher shock velocity produced more fragments. The great majority of fragments was within $0-10\,\mathrm{nm}^3$, which was more in the NC model than the SC model; in addition, the large fragments were considerably fewer.

Statistics revealed that there were very few fragments, most of which were in the range of $0-10\,\mathrm{nm}^3$. From the whole volume size, our results agreed well with the MD results of Durand and Soulard [36]. More importantly, in Fig. 13 and Fig. S8 in the Supplemental Material [41], a red trendline was added within the range of $0-40\,\mathrm{nm}^3$ in the snapshot at $t = 100$ ps, which shows that the fragment statistics followed a power law expressed as $N_f \propto V^{-n}$, where n is the decay factor. This result is consistent with the size distribution of Cu and Sn ejecta [35,36]. The SC model at $u_p = 3$ km/s and NC model at $u_p = 4$ km/s exhibited identical distribution laws for fragments within $0-40\,\mathrm{nm}^3$, which was not suitable for the SC and NC models at $u_p = 5$ km/s. The decay factor n for the SC models at $u_p = 3$ and 4 km/s was 2.0, while for the NC model at $u_p = 4$ km/s, it was 0.85, which was basically in accordance with 1.15 ± 0.08 [36].

IV. DISCUSSION

As previously found, spallation and microjetting were observed to coexist at $u_p = 2-5$ km/s. It is particularly worth noting that the spallation emergence might cause the jet to dissipate or accelerate the fracture process. Thus, in this section, we primarily address the mutual interaction between spallation and microjetting, namely, the influence of spallation on jet disappearance and rapid fracture.

First, it needs to be pointed out that the term *disappearance* includes the incomplete and complete ones here. The microjet will typically evolve from linear growth to nonlinear growth and ultimately break into fragments if it is formed. However, concurrent with the spallation, a unique jet evolution from formation, growth, arrest, retrogression to disappearance occurs at $u_p = 2$ and 3 km/s. Consequently, there must be some correlation between spallation and microjetting.

In Fig. 14(a), since the model was in an initial tensile state, there were no voids, while the spike entered a linear increase stage at $t = T_1 - T_2$. When the spike was in a nonlinear increase stage at $t = T_2 - T_3$, the voids had undergone nucleation, growths, collapse, and coalescence; like the SC spallation model at $u_p = 2$ km/s, the voids were confined to a very thin zone, as shown in Fig. 6(b). With the partial separation between the matrix bulk and spalled layer, the spike length began to decrease at $t = T_3 = 34.0$ ps, indicating its retrogression beginning. At $t = T_4 = 47.0$ ps, the spike length transformed from a slow decrease to a rapid decrease, and the spalled layer was partly connected with the matrix bulk through some thin ligaments, which could be inferred from the snapshots in Fig. 7(b). The spike showed a complete retrogression at $t = T_5 = 61.0$ ps, which demonstrated the concurrent spallation and microjetting retrogressed to the pure spallation behavior.

Like the SC Al case at $u_p = 2$ km/s, the spike length increased linearly at $t = T_1 - T_2$ in Fig. 14(b). The NC Al

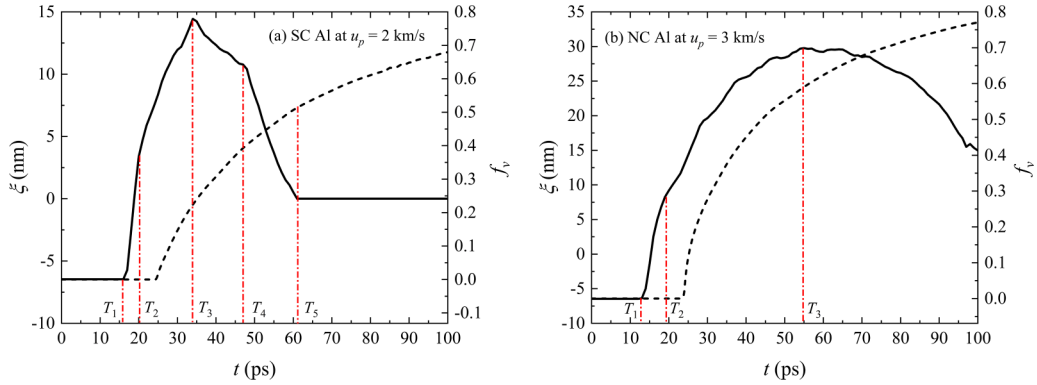

FIG. 14. The evolutionary comparison between spike length ξ and void volume fraction f_v in the spallation zone, where the solid and dashed curves represent ξ and f_v.

model did not generate the voids at $u_p = 3$ km/s; instead, the voids nucleated, grew, collapsed, and coalesced at $t = T_2 - T_3$, which corresponded to a nonlinear increase stage of the spike length. The spike started to retrogress after $t = T_3 = 55.0$ ps, its length dropped nonlinearly, and it presented an incomplete disappearance at $t = 100.0$ ps.

Both scenarios share that void nucleation, growth, collapse, and coalescence occurred during the nonlinear rise stage of the spike. When the spike length reached its maximum, the coalescence was basically complete, and the model began to separate the spalled layer containing the ejecta from the matrix. The stress wave that reached the spalled layer containing the jet would be cut off by separation, whereas the residual stress wave energy within the layer was comparatively minimal, thereby posing challenges to the ongoing jet development. There were no more new atoms to replenish the tail of the jet throughout the separation process since there was no longer any continuous loading of stress waves. This phenomenon tended toward a steady state since no additional atoms were ejected from the surface to form the jet. The velocity of the jet head would drop because of the dragging effect of the jet tail on it. Only in terms of the moving velocity, if the bubble and spike velocities were respectively greater than and less than the free surface velocity, could the spalled layer gradually merge into the bubble and spike. When the free surface, bubble, and spike fully merge into one, it indicates the complete disappearance of the spike.

According to the melting results [44], interfacial Richtmyer-Meshkov flow in the SC Al model at $u_p = 2$ km/s was solid, but it was liquid in the NC Al model at $u_p = 3$ km/s. Indeed, the elevated temperature within the medium that resulted from shock wave loading was not immediately apparent. As the intensity of the shock wave disturbance increased, the spike underwent further plastic deformation. The increase in temperature resulting from the conversion of plastic work and adiabatic shock was inadequate to initiate the melting of the medium. Furthermore, the solid tensile strength of the ejecta made it exceedingly challenging to induce a tensile fracture. Here, the tensile strength might be considered one of the tensile-dragging effects, while for the liquid flow, it shared a similar disappearance mechanism with the solid flow. The tensile strength induced by the velocity gradient should be lower than the critical liquid one that resulted in ejecta breakup, allowing the ejecta to maintain nonbreaking.

To recapitulate, the radical cause of jet disappearance or retrogression is that the energy of the stress wave is cut off by spallation formation, resulting in no fresh atoms joining the jet.

In general, during the only jet breakup process, the complete breakup from head to tail takes several hundred picoseconds and even >1 ns in MD simulations [34,35], with tail breakup being especially difficult due to the continuous particle injection. The fragmentation of the only microjet does not consider the spallation influence, which contrasts with our observations of the fragmentation behavior within 100 ps in this paper. Thus, the spallation formation has contributed to the jet fragmentation. However, the physics of the accelerated fragmentation induced by spallation remains unknown.

According to the sequential occurrence of the jet fragmentation at $u_p = 3{-}5$ km/s, it is found that the breakup of the liquid jet is slightly ahead of the void nucleation in the spallation zone, as shown in Fig. S5 in the Supplemental Material [41]. That is to say, the unstable growth of the jet occurs before the spallation. It is generally known that a higher shock velocity allows more energy of the compressive stress wave to enter the jet, generating a larger velocity gradient and consequent tensile stress, which in turn leads to the void NAG in the jet. Thus, the velocity gradient is responsible for the early breakup. Following that, the jet breakup and void evolution in the spallation zone seem to independently develop. Void growth and coalescence within the spallation zone serve to obstruct the energy of the stress wave from entering the spalled layer, thereby inhibiting the particles from forming the jet tail. Moreover, they also effectively trap the energy of the stress wave from escaping the jet, just allowing stress waves to oscillate in the spalled layer containing the jet. Consequently, this accelerates the fragmentation process of the jet. When the separation between the spalled layer and matrix bulk is complete, the breakup has extended to the tail. The spalled layer with a relatively higher velocity, on the one hand, assimilates the disconnected fragments within ~40 nm between the free surface and the fragment [34]; on the other hand, it also takes in the residual fragments connected with the free surface, and this uneven free face will be transformed into a flat one under the effects of surface tension and viscosity. These jet behaviors were also observed in metal Sn [34].

Additionally, it should be noted that there is a critical transition for the disappearance and accelerated fragmentation of the jet. The critical shock velocity ranges from 1 to 2 km/s for the SC model and from 2 to 3 km/s for the NC model, respectively. Lastly, the transition criterion, as our next research focus, will be studied in the future.

V. CONCLUSIONS

In this paper, MD simulations were performed to investigate the coupling behaviors of spallation and microjetting in SC and NC Al. The main findings are

(1) The complete micromechanisms of ductile fracture are dominated by void nucleation, growth, collapse, and coalescence. Compressive collapse and spontaneous collapse are two typical void collapse mechanisms, with a peculiar behavior that a coalesced void can also collapse. Moreover, the radius of a collapsed void exhibits a rapid increase at first, a moderate decrease later, and finally a quick decline.

(2) Spallation can lead to the disappearance and accelerated fragmentation of the microjet. The grain boundary not only limits the microjet growth owing to energy dissipation, but it also causes a higher peak velocity of the spike tip than the SC microjetting model due to the inhomogeneous deformation.

(3) Void growth and coalescence in the spallation zone prevent the stress wave energy from entering the microjet body and particle source to inject the jet tail. This effectively restrains the nonlinear jet growth, leading to the arrest, retrogression, and disappearance of the microjet in sequence. As a result, the coexisting microjetting and spallation convert into a single spallation.

(4) The jet sheet fragmentation is dominated by three mechanisms: void nucleation, growth, and coalescence for the jet body; longitudinal necking induced by the tensile stress for the residual one-dimensional jet body; and transverse necking induced by the shear and tensile stresses for the jet head. In addition, for small-sized fragments, the relation of number vs volume follows a power-law distribution.

ACKNOWLEDGMENTS

This paper was supported by the National Natural Science Foundation of China (Grants No. 12202081, No. 12372367, and No. 12172313), the Shock and Vibration of Engineering Materials and Structures Key Laboratory of Sichuan Province (Grant No. 20kfgk02), and the Doctoral Foundation of Southwest University of Science and Technology (Grant No. 23zx7176).

[1] W. T. Buttler, R. J. R. Williams, and F. M. Najjar, Foreword to the special issue on ejecta, J. Dyn. Behav. Mater. **3**, 151 (2017).

[2] V. A. Ogorodnikov, A. L. Mikhailov, V. V. Burtsev, S. A. Lobastov, S. V. Erunov, A. V. Romanov, A. V. Rudnev, E. V. Kulakov, Yu. B. Bazarov, V. V. Glushikhin *et al.*, Detecting the ejection of particles from the free surface of a shock-loaded sample, J. Exp. Theor. Phys. **109**, 530 (2009).

[3] D. B. Holtkamp, D. A. Clark, E. N. Ferm, R. A. Gallegos, D. Hammon, W. F. Hemsing, G. E. Hogan, V. H. Holmes, N. S. P. King, R. Liljestrand *et al.*, A survey of high explosive-induced damage and spall in selected metals using proton radiography, AIP Conf. Proc. **706**, 477 (2004).

[4] T. J. Voglera and J. D. Clayton, Heterogeneous deformation and spall of an extruded tungsten alloy: Plate impact experiments and crystal plasticity modeling, J. Mech. Phys. Solids **56**, 297 (2008).

[5] A. Sher, L. Meshi, S. Kalabukhov, N. Frage, and E. B. Zaretsky, Shock wave determination of temperature dependence of twinning stress in vanadium and tantalum, Mater. Sci. Eng. A **833**, 142537 (2022).

[6] A. R. Cui, S. C. Hu, S. Zhang, J. C. Cheng, Q. Li, J. Y. Huang, and S. N. Luo, Spall response of medium-entropy alloy CrCoNi under plate impact, Int. J. Mech. Sci. **252**, 108331 (2023).

[7] P. T. Steele, B. A. Jacoby, S. M. Compton, and J. O. Sinibaldi, Advances in ejecta diagnostics at LLNL, J. Dyn. Behav. Mater. **3**, 253 (2017).

[8] M. M. Schauer, W. T. Buttler, D. K. Frayer, M. Grover, B. M. LaLone, S. K. Monfared, D. S. Sorenson, G. D. Stevens, and W. D. Turley, Ejected particle size distributions from shocked metal surfaces, J. Dyn. Behav. Mater. **3**, 217 (2017).

[9] J. R. Asay, L. P. Mix, and F. C. Perry, Ejection of material from shocked surfaces, Appl. Phys. Lett. **29**, 284 (1976).

[10] W. T. Buttler, M. B. Zellner, R. T. Olson, P. A. Rigg, R. S. Hixson, J. E. Hammerberg, A. W. Obst, J. R. Payton, A. Iverson, and J. Young, Dynamic comparisons of piezoelectric ejecta diagnostics, J. Appl. Phys. **101**, 063547 (2007).

[11] J. A. Don Jayamanne, J.-R. Burie, O. Durand, R. Pierrat, and R. Carminati, Characterization of ejecta in shock experiments with multiple light scattering, J. Appl. Phys. **135**, 073105 (2024).

[12] T. M. Hartsfield, R. K. Schulze, B. M. La Lone, J. J. Charonko, J. E. Hammerberg, J. D. Regele, M. M. Schauer, J. D. Schwarzkopf, D. G. Sheppard, G. D. Stevens *et al.*, The temperatures of ejecta transporting in vacuum and gases, J. Appl. Phys. **131**, 195104 (2022).

[13] D. S. Sorenson, G. A. Capelle, M. Grover, R. P. Johnson, M. I. Kaufman, B. M. LaLone, R. M. Malone, B. F. Marshall, R. W. Minich, P. D. Pazuchanics *et al.*, Measurements of Sn ejecta particle-size distributions using ultraviolet in-line Fraunhofer holography, J. Dyn. Behav. Mater. **3**, 233 (2017).

[14] D. R. Curran, L. Seaman, and D. A. Shockey, Dynamic failure of solids, Phys. Rep. **147**, 253 (1987).

[15] T. Autoun, L. Seaman, D. R. Curran, G. I. Kanel, S. V. Razorenov, and A. V. Utkin, *Spall Fracture* (Springer, New York, 2002).

[16] S. N. Luo, T. C. Germann, T. G. Desai, D. L. Tonks, and Q. An, Anisotropic shock response of columnar nanocrystalline Cu, J. Appl. Phys. **107**, 123507 (2010).

[17] E. B. Zaretsky and G. I. Kanel, Effect of temperature, strain, and strain rate on the flow stress of aluminum under shock-wave compression, J. Appl. Phys. **112**, 073504 (2012).

[18] P. B. Trivedi, J. R. Asay, Y. M. Gupta, and D. P. Field, Influence of grain size on the tensile response of aluminum under plate-impact loading, J. Appl. Phys. **102**, 083513 (2007).

[19] J. P. Escobedo, D. Dennis-Koller, E. K. Cerreta, B. M. Patterson, C. A. Bronkhorst, B. L. Hansen, D. Tonks, and R. A. Lebensohn, Effects of grain size and boundary structure on the dynamic tensile response of copper, J. Appl. Phys. **110**, 033513 (2011).

[20] S. J. Fensin, J. P. Escobedo-Diaz, C. Brandl, E. K. Cerreta, G. T. Gray III, T. C. Germann, and S. M. Valone, Effect of loading direction on grain boundary failure under shock loading, Acta Mater. **64**, 113 (2014).

[21] M. Cheng, C. Li, M. X. Tang, L. Lu, Z. Li, and S. N. Luo, Intragranular void formation in shock-spalled tantalum: Mechanisms and governing factors, Acta Mater. **148**, 38 (2018).

[22] A. E. Mayer and P. N. Mayer, Evolution of pore ensemble in solid and molten aluminum under dynamic tensile fracture: Molecular dynamics simulations and mechanical models, Int. J. Mech. Sci. **157**, 816 (2019).

[23] X. Yang, J. L. Cheng, H. Zhao, and F. Wang, Nanovoid collapse mechanism in defect-free aluminum under isothermal and adiabatic conditions, Scr. Mater. **235**, 115590 (2023).

[24] M. B. Zellner, G. Dimonte, T. C. Germann, J. E. Hammerberg, P. A. Rigg, G. D. Stevens, W. D. Turley, and W. T. Buttler, Influence of shockwave profile on ejecta, AIP Conf. Proc. **1195**, 1047 (2009).

[25] J. L. Shao, P. Wang, and A. M. He, Microjetting from a grooved Al surface under supported and unsupported shocks, J. Appl. Phys. **116**, 073501 (2014).

[26] X. Yang, H. Zhao, X. J. Gao, G. Lei, and Z. L. Chen, Molecular dynamics study on micro jet in single crystal aluminum, Acta Mech. Sin. **39**, 122232 (2023).

[27] W. T. Buttler, R. S. Hixson, N. S. P. King, R. T. Olson, P. A. Rigg, M. B. Zellner, N. Routley, and A. Rimmer, Method to separate and determine the amount of ejecta produced in a second-shock material-fragmentation event, Appl. Phys. Lett. **90**, 151921 (2007).

[28] B. Wu, A. M. He, X. X. Wang, H. Q. Sun, and P. Wang, Numerical investigation of ejecta mass of twice-shocked liquid Sn, J. Appl. Phys. **133**, 165903 (2023).

[29] D. J. Bell, N. R. Routley, J. C. F. Millett, G. Whiteman, M. A. Collinson, and P. T. Keightley, Investigation of ejecta production from tin at an elevated temperature and the eutectic alloy lead–bismuth, J. Dyn. Behav. Mater. **3**, 208 (2017).

[30] W. T. Buttler, S. K. Lamoreaux, R. K. Schulze, J. D. Schwarzkopf, J. C. Cooley, M. Grover, J. E. Hammerberg, B. M. La Lone, A. Llobet, R. Manzanares *et al.*, Ejecta transport, breakup and conversion, J. Dyn. Behav. Mater. **3**, 334 (2017).

[31] D. Y. Jin, X. L. Deng, and W. Y. Liu, Eulerian peridynamic modeling of microjetting from a grooved aluminum sample under shock loading, J. Appl. Phys. **131**, 105108 (2022).

[32] G. Dimonte, G. Terrones, F. J. Cherne, and P. Ramaprabhu, Ejecta source model based on the nonlinear Richtmyer-Meshkov instability, J. Appl. Phys. **113**, 024905 (2013).

[33] F. Wang, J. Liu, A. M. He, P. Wang, and J. G. Wang, Ejecta production from metal Sn into inert gases, J. Appl. Phys. **127**, 195901 (2020).

[34] O. Durand and L. Soulard, Mass-velocity and size-velocity distributions of ejecta cloud from shock-loaded tin surface using atomistic simulations, J. Appl. Phys. **117**, 165903 (2015).

[35] A. M. He, P. Wang, and J. L. Shao, Heterogeneous fragmentation of metallic liquid microsheet with high velocity gradient, Chin. Phys. B **25**, 017102 (2016).

[36] O. Durand and L. Soulard, Power law and exponential ejecta size distributions from the dynamic fragmentation of shock-loaded Cu and Sn metals under melt conditions, J. Appl. Phys. **114**, 194902 (2013).

[37] C. Roland, T. de Rességuier, A. Sollier, E. Lescoute, L. Soulard, and D. Loison, Hydrodynamic simulations of microjetting from shock-loaded grooves, AIP Conf. Proc. **1793**, 100027 (2017).

[38] M. Y. Xu, W. D. Song, C. Wang, P. Wang, J. L. Shao, and E. L. Tang, Theoretical and experimental study on the hypervelocity impact induced microjet from the grooved metal surface, Int. J. Impact Engng. **156**, 103944 (2021).

[39] J. M. Winey, A. Kubota, and Y. M. Gupta, A thermodynamic approach to determine accurate potentials for molecular dynamics simulations: Thermoelastic response of aluminum, Model. Simul. Mater. Sci. Eng. **17**, 055004 (2009).

[40] X. Yang, X. G. Zeng, J. Wang, J. B. Wang, F. Wang, and J. Ding, Atomic-scale modeling of the void nucleation, growth, and coalescence in Al at high strain rates, Mech. Mater. **135**, 98 (2019).

[41] See Supplemental Material at http://link.aps.org/supplemental/10.1103/PhysRevB.110.024113 for more details about the evolutionary processes of spallation and microjetting as well as statistical data about the void radius, void volume fraction, and fragment.

[42] F. Q. Zhao, X. B. Ma, H. Pan, and J. X. Liu, Modeling of dynamic elasto-plastic growth of a nano-void with surface energy, inertia and thermal softening effects, AIP Adv. **9**, 105313 (2019).

[43] F. C. Wu, Y. B. Zhu, X. Z. Li, P. Wang, Q. Wu, and H. A. Wu, Peculiarities in breakup and transport process of shock-induced ejecta with surrounding gas, J. Appl. Phys. **125**, 185901 (2019).

[44] X. Yang, X. G. Zeng, F. Wang, J. Ding, H. Zhao, and B. Xue, Spallation fracture dependence on shock intensity and loading duration in single-crystal aluminum, Comput. Mater. Sci. **210**, 111060 (2022).